Department of Physics and Astronomy

University of Heidelberg

Master thesis

in physics

submitted by

Dominick Cichon

born in Mannheim (Germany)

2015

Identifying ^{222}Rn decay chain events in liquid xenon detectors

This master thesis has been carried out by Dominick Cichon

at the

Max-Planck-Institut für Kernphysik

under the supervision of

Frau Priv.-Doz. Teresa Marrodán Undagoitia

Das Identifizieren von Ereignissen der ^{222}Rn-Zerfallsreihe in Flüssigxenon-Detektoren:

Auf der Suche nach Dunkler Materie wurden im Laufe der letzten Jahre Detektoren gebaut, die flüssiges Xenon als Detektionsmedium verwenden. Für diese stellen ^{222}Rn und dessen Tochternuklide eine gefährliche Untergrundquelle dar, da sie Signale verursachen können, die denen ähneln, die man von Teilchen der Dunklen Materie erwarten würde. Dementsprechend ist es wichtig, zu verstehen, wie Signale der ^{222}Rn-Zerfallsreihe identifiziert werden können. Aufgrund dessen ist diese Arbeit der Suche nach solchen Signalen in zwei Detektoren gewidmet. Einer dieser Detektoren ist XENON100, der zu den führenden Experimenten zum direkten Nachweis von Dunkler Materie zählt. In diesem Fall werden Ereignisse der ^{222}Rn-Zerfallsreihe dazu verwendet, um die Effektivität von Destillationstechniken zur Trennung von Radon und Xenon zu quantifizieren. Der andere Detektor heißt HeidelbergXenon (HeXe), und wurde vor Kurzem am Max-Planck-Institut für Kernphysik gebaut, um die Zerfälle von ^{222}Rn und seiner Tochternuklide in flüssigem Xenon zu untersuchen. Um eben dies zu bewerkstelligen, wird im Laufe dieser Arbeit ein Datenprozessor entwickelt und getestet. Ebenso werden die elektronischen Komponenten und die Photosensoren, die für Messungen mit HeXe verwendet werden, charakterisiert. Zum Schluss werden HeXe Daten, die mit radon-angereichertem Xenon aufgenommen wurden, analysiert, um nach Ereignissen der ^{222}Rn-Zerfallsreihe zu suchen.

Identifying ^{222}Rn decay chain events in liquid xenon detectors:

In the search for dark matter, detectors have been built over the last years which use liquid xenon as a detection medium. For them, ^{222}Rn and its daughter nuclides pose a dangerous background source, as they can cause signals which look like those expected from dark matter particles. Consequently, it is important to understand, how ^{222}Rn decay chain signals can be identified. As a result, this thesis is dedicated to looking for such signals in two detectors. One of them is the XENON100 detector, which belongs to the leading dark matter direct detection experiments. ^{222}Rn decay chain event rates are used here for quantifying the effectiveness of using distillation techniques to separate radon from xenon. The other detector is called HeidelbergXenon (HeXe), and has been recently built at the Max-Planck-Institut für Kernphysik in order to study the decays of ^{222}Rn and its daughter nuclides in liquid xenon. To achieve this task, a data processor is developed and tested over the course of this thesis. Also, the electronics equipment as well as the photosensors used for measuring with HeXe are characterized. Finally, HeXe data, taken with radon-enriched xenon, is analyzed to look for ^{222}Rn decay chain events.

Contents

Glossary

ASCII	American Standard Code for Information Interchange
BiPo	bismuth polonium
BSM	beyond the Standard Model
DAQ	data acquisition
DAX	Data Acquisition for XENON100
GXe	gaseous xenon
HeXe	HeidelbergXenon
LNGS	Laboratori Nazionali del Gran Sasso
LXe	liquid xenon
MFC	mass flow controller
MPIK	Max-Planck-Institut für Kernphysik
PE	photoelectron
PMT	photomultiplier tube
PTFE	polytetrafluoroethylene
QE	quantum efficiency
SI	Système international d'unités
SPE	single-photoelectron
TPC	time projection chamber

WIMP	Weakly Interacting Massive Particle
xerawdp	XENON Raw Data Processor
ZLE	zero length encoding

1. Introduction

Motivated by astrophysical observations, liquid xenon (LXe) detectors are being built to search for hypothetical dark matter particles. Because interactions of these particles with known matter are expected to be rare, detectors must operate at ultra-low background conditions to remain sensitive. One of the principal background sources is ^{222}Rn. As such, it is important to understand, how detector signals generated by the decay of ^{222}Rn and its daughter nuclides look like.

Therefore, this thesis aims to identify ^{222}Rn decay chain events in two different LXe detectors. One of them is XENON100 [1] (described in chapter 2), for which radon event rates are determined to estimate the amount of background within the detector's region of interest. Rates also need to be known in order to quantify, how effective distillation techniques are in separating radon from xenon, as corresponding tests are conducted with XENON100 (see chapter 3). The other one, called HeidelbergXenon (HeXe) (described in chapter 4), is a newly built detector at the Max-Planck-Institut für Kernphysik (MPIK), which is used for studying ^{222}Rn and its daughters in LXe. In order to demonstrate, that HeXe, in combination with a data processor written for this thesis, can reliably detect radon events, measurements with radon-enriched xenon are conducted and analyzed (see chapter 5).

In this context, the current chapter motivates the construction of LXe detectors for dark matter detection. In addition, the importance of ^{222}Rn and its daughter nuclides for such experiments is explained.

1.1. The search for dark matter

Beginning with observations conducted by Fritz Zwicky in the 1930s [2], more and more evidence for the universe containing an invisible mass component, called "dark matter", was gathered over the course of the last century. Vera C. Rubin, for example, found out [3], that the velocity of stars orbiting within the Andromeda Galaxy does

not fall off with increasing distance to the galactic nucleus, as it would be expected by Newtonian mechanics, but instead remains constant. A solution to explain the higher-than-expected rotation velocities at large distances from the galactic center would be to assume a halo of dark matter.

Possibly the most striking evidence for dark matter to exist is given by observations of the cosmic microwave background. The power spectrum of its anisotropy, as observed by Planck [4] and similar missions, can only be explained by assuming a non-baryonic dark matter component in the universe, which does not interact via electromagnetic interactions and makes up 84 % of the universe's entire matter content. This rules out many Standard Model particles. Dark matter also cannot interact via the strong force, as it would have been observed by now if it would. When considering the fact, that dark matter needs to be stable over cosmological timescales to affect the evolution of galaxies, only neutrinos remain as Standard Model candidates. However, they cannot make up a majority of dark matter, as they were created at relativistic speeds during the big bang, while large-scale simulations of the universe [5] show, that a non-relativistic dark matter component has to exist in order to explain the observed evolution of the universe.

In conclusion, there is strong evidence for dark matter to be only explainable by physics beyond the Standard Model (BSM). At the time of writing, Weakly Interacting Massive Particles (WIMPs), which meet all of the above requirements for dark matter, are one of the most promising candidates [6]. One of the reasons for this is, that such particles are already predicted by popular BSM theories like Supersymmetry [7]. As they have to couple to ordinary matter, there are three principal ways of detecting them [6]: First, one can detect particles resulting from the annihilation of WIMPs pairs. For example, space detectors like the Fermi Gamma-ray Space Telescope [8] and AMS [9] are looking for this kind of signal. Second, one can look fo WIMPs being produced in particle collisions. ATLAS and CMS have already turned their attention towards this kind of interaction [10, 11].

Finally, WIMPs are also expected to scatter elastically off regular matter. Experiments looking for such a signal are called "direct detection experiments". While cryogenic bolometers provide the best limits for WIMP masses up to 6 GeV/c [14], the field of direct detection is, for larger masses, largely driven by LXe detectors like XENON100 [1] and LUX [15], which currently provide the most restrictive limits on the allowed WIMP parameter space for WIMP masses larger than 6 GeV/c [16, 17]. (figure 1.1). The reasons for why LXe is a popular choice for direct detection experiments are

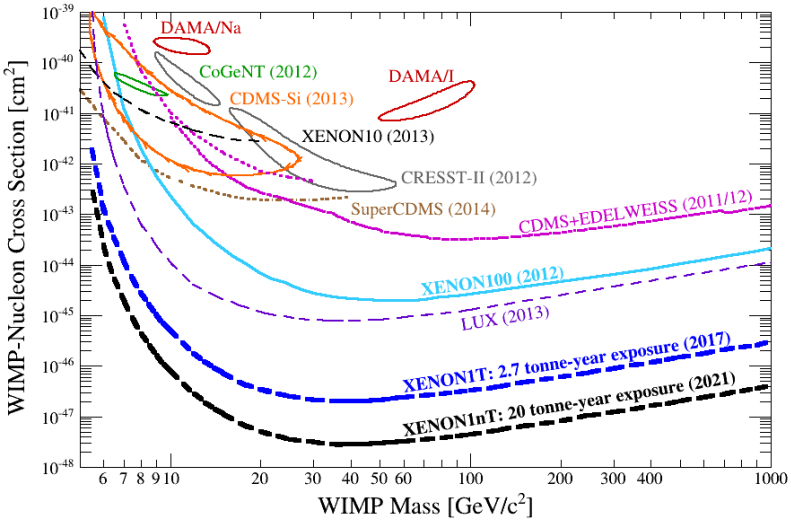

Figure 1.1.: Selection of limits for the spin-independent WIMP-nucleon interaction cross-section [12]. Included are predictions for the future experiments XENON1T [13] and its proposed upgrade, XENON1nT. Regions of the parameter space below a limit line are excluded. Closed areas denote best-fit regions for experiments which claim to have observed dark matter interactions.

outlined in the following section.

1.2. Liquid xenon as an active medium for particle detection

Xenon is one of the heaviest noble gases, possessing a high nuclear charge ($Z = 54$ [18]). Consequently, it offers high stopping power when liquefied [19]. Another advantage is, that it provides a homogenous detection volume with a relatively high density ($\rho \approx 3\,\mathrm{g/cm^3}$ [18]) [19].

One of the most important features of LXe is, that particles interacting with it produce scintillation photons *and* charge carriers at the same time[1] [19] (see figure 1.2). Charge carrier production occurs via ionization of xenon atoms, with an average energy of $W = (15.6 \pm 0.3)\,\mathrm{eV}$ being required for the creation of an electron-ion pair [19]. Scintillation photons, on the other hand, are the result of a more complex process: Via direct interaction and recombination of ionized xenon with electrons, excited xenon atoms are generated. Pairs of such excited xenon atoms then form excimers (Xe_2^*),

[1] A fraction of the deposited energies is also converted to heat [20].

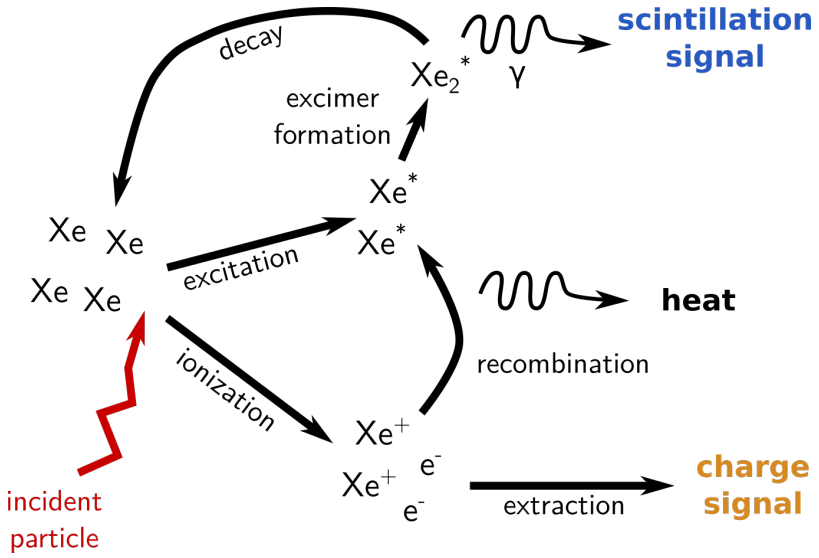

Figure 1.2.: Illustration of how charge and scintillation signals are generated in LXe. Note the interdependence between charge and scintillation signals, which encodes additional information about a particle interaction [19]. The generated heat can, in principle, also be used as a signal, but it is not important for the detectors this thesis focuses on.

which decay under emission of photons at an average wavelength of $\lambda = 177.6\,\mathrm{nm}$ [19]. This corresponds to a photon energy which is too low to excite xenon, making LXe transparent to its own scintillation light [20]. In addition, the scintillation signal response time is fast, as the processes involved happen on a timescale of $\mathcal{O}(20\,\mathrm{ns})$ [19]. In the end, the average energy needed to create a scintillation photon is at the order of $\mathcal{O}(20\,\mathrm{eV})$, and depends on the type of the interacting particle [19].

Because electron-ion recombination is a process culminating in the creation of scintillation photons, the amount of free charge carriers and the number of scintillation photons are anti-correlated. Experiments sensitive to both are thus able to increase their energy resolution by combining the two signals [19]. In addition, as the electron-ion recombination rate and thus the ratio between scintillation and charge signal depends on the type of the interacting particle, it also allows for interaction type discrimination.

In the context of WIMP detection, interaction type discrimination is crucial, as it allows to discriminate nuclear recoils, which WIMPs are expected to cause, against electronic recoils, which result from background sources [1].

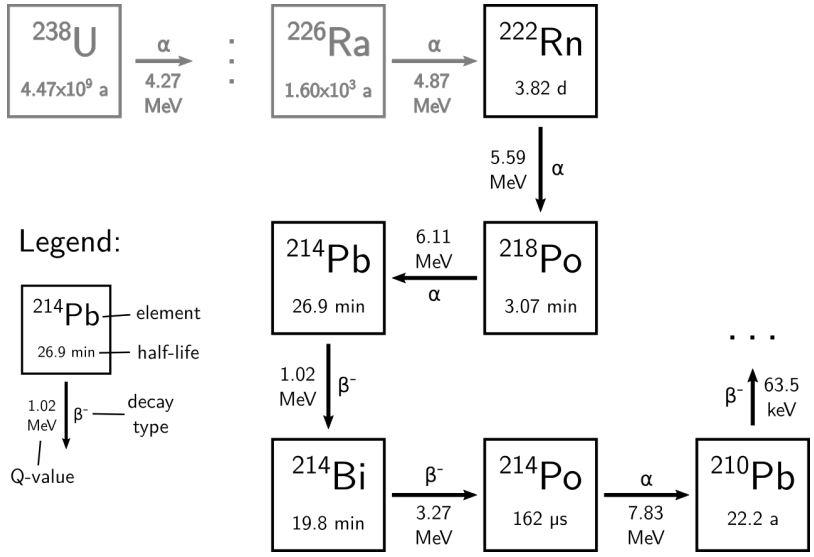

Figure 1.3.: Excerpt of the ^{238}U decay chain, which shows the decays of the ^{222}Rn sub-chain that are most relevant for dark matter direct detection experiments. Rare decays with a branching ratio smaller than 1 % have been omitted. All values shown are from [23].

1.3. ^{222}Rn as a background source in liquid xenon dark matter experiments

One of the most important of these sources is radon, the only naturally occurring noble gas which does not possess stable isotopes [21] [22, chapter 04]. Its most abundant isotope, ^{222}Rn, originates from the decay of ^{226}Ra, which in turn is produced by the decay of primordial ^{238}U. It has a half-life of 3.82 d [23]. This half-life is sufficiently long for it to be able to diffuse into a LXe detector before having started to decay into shorter-lived daughter nuclides. In addition, trace amounts of ^{238}U and ^{226}Ra within detector materials cause them to emanate ^{222}Rn into the detector volume. As it is a noble gas and has properties similar to xenon, it is difficult to separate them [22, section 4.2].

The decay chain of ^{222}Rn is illustrated in figure 1.3, up to including ^{210}Pb. Subsequent elements are not relevant for dark matter experiments, as the half-life of ^{210}Pb is long compared to the usual time an experiment is running ($T_{1/2} = 22.23$ a [23]). The α-decays do not pose a problem, as the energies of the resulting α-particles cause signals much larger than those expected from WIMP interactions. However, the chain's β-decays are dangerous, as they increase the amount of the electronic recoil

background. While discrimination against such interactions is offered by LXe if an experiment is sensitive to both scintillation and charge, it is impossible to completely reject background interactions due to statistical fluctuations, by which electronic recoil events might leak into the signal region one is interested in. For the XENON100 experiment, the rate of such background events in the region of interest for WIMP signals is estimated to be around 5.1×10^{-3} events/kg/day/keV. ^{222}Rn makes out 42 % [24, section 1.2.2] of it, which illustrates the huge influence ^{222}Rn can have on background rates.

As a consequence, several actions are taken to handle the ^{222}Rn background. First, extensive screening campaigns are carried out to only select low-radioactivity components for the detector [24]. Second, events caused by ^{222}Rn chain decays which possess distinctive signatures are identified and rejected. An example for this is the β-decay of ^{214}Bi, which can be identified by its coincidence with the α-decay of ^{214}Po that follows shortly afterwards ($T_{1/2} = 162.3\,\mu s$ [23], see also chapter 3). Third, the total amount of ^{222}Rn in the detector is estimated by determining the rates of identifiable decay chain decays occurring in the detector. This is necessary, because temporal isolated β-decays, like the one of ^{214}Pb, might look exactly like WIMP interactions. Consequently, they cannot be effectively rejected in this case.

To decrease the influence of ^{222}Rn even further, new techniques for reducing radon contencration levels are being developed and tested. Using XENON100 as a test case, the usage of a distillation column to separate radon and xenon has been probed recently [25]. A short overview of XENON100 itself and the setup employed for testing distillation is given in the next chapter.

2. The XENON100 experiment

XENON100 is a dark matter direct detection experiment, located in the underground laboratories of the Laboratori Nazionali del Gran Sasso (LNGS) in Italy, where it is shielded from cosmic radiation by a layer of about 1.4 km of rock [26]. It uses LXe as a detection medium, employing a dual-phase time projection chamber (TPC) design. This allows it to be sensitive to both charge and scintillation signals (see section 1.2), enabling it do discriminate particle interaction types as well as to fully reconstruct the location of a particle interaction [1]. XENON100 provided, until the publishment of more recent results by LUX [17], the strictest limits on the allowed parameter space for WIMP interactions [16].

This chapter outlines the general detection principle of the XENON100 detector. A description of the TPC and the data acquisition (DAQ) equipment is given (see also [1]). Following that, the test setup for probing distillation techniques, as mentioned at the end of the previous chapter, is elaborated on.

2.1. Time projection chamber (TPC)

The XENON100 dual-phase TPC, as seen in figure 2.1, measures about 30.5 cm in height and 30.6 cm in diameter, being almost cylindrical. It encloses a volume containing 62 kg of LXe, which is delimited by reflective polytetrafluoroethylene (PTFE) panels acting as the TPC's side walls, and optically transparent metal meshes to its top and bottom. The meshes consist of a cathode mesh, marking the bottom boundary, and a stack of an anode mesh positioned between two grounded meshes (top mesh stack), which denotes the top boundary of the TPC. They, together with field shaping electodes that are mounted on the PTFE panels, generate a homogenous drift field of 0.53 kV/cm across the TPC volume. The field is polarized such, that negative charge carriers drift towards the top, with the drift velocity for electrons being 1.73 mm/µs.

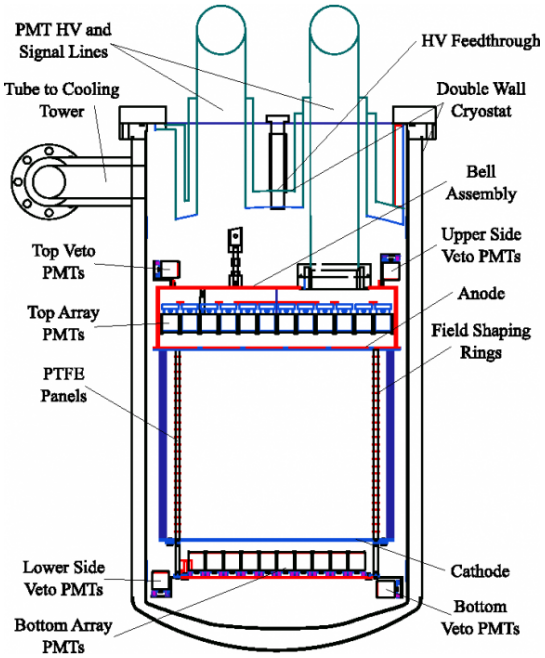

Figure 2.1.: Diagram of the XENON100 TPC and cryostat [1].

Located above and below the TPC are photomultiplier tube (PMT) arrays containing 178 Hamamatsu R8520-06-Al [27] PMTs in total. The bottom array is completely submerged in LXe and contains 80 PMTs. It is positioned below the cathode mesh, being protected from the cathode high voltage by a grounded screening mesh. The top array contains 98 PMTs and is located within a pressurized diving bell, in which a gaseous xenon (GXe) atmosphere is maintained. The bell design allows for a precise control of the liquid level inside the TPC by varying the GXe pressure. Directly below the upper PMT array, charge carriers from particle interactions are extracted out of the LXe volume into the GXe phase by an extraction field of approximately 12 kV/cm, which is created by the top mesh stack. As the charge carriers enter the GXe atmosphere and are accellerated by the extraction field, they generate proportional scintillation light, which is detected by the PMTs.

The entire TPC is surrounded by 99 kg of LXe. 64 PMTs mounted on the TPC's outside observe the outer LXe volume, which acts both as a passive shield, due to the high stopping power of LXe, and as an active veto. Both volumes are optically separated.

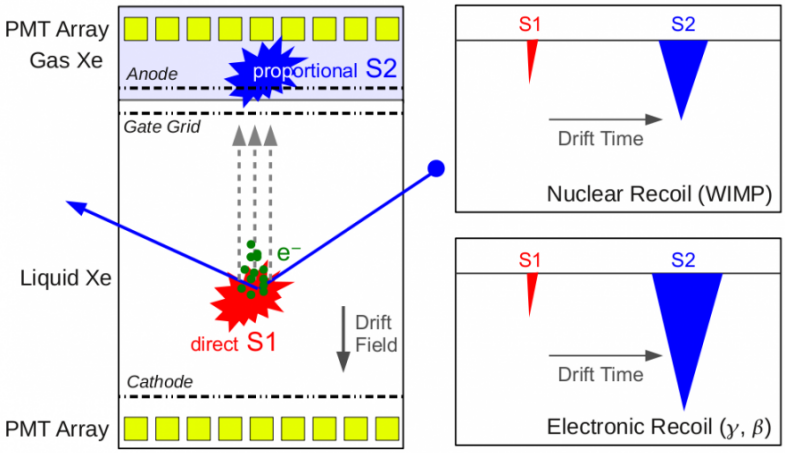

Figure 2.2.: Schematic outlining the working principle of the XENON100 TPC, originally from [1]. (Left) An illustration of how the prompt scintillation (S1) as well as the charge signal (S2) is generated. (Right) A sketch showing, how the sizes of S1 and S2 signals relative to each other differ between nuclear recoils, which WIMPs are hypothesized to cause, and electronic recoils, which are caused by background particles.

2.2. Detection principle

Particle interactions inside the TPC are detected as follows: An incident particle interacts with the LXe volume and produces both scintillation photons as well as ionization electrons (see figure 2.2, left, and section 1.2). The scintillation light is directly detected by the PMTs and produces the so-called "S1" signal. Because of the drift field, the electrons move towards the phase boundary between LXe and GXe, where they are extracted by the extraction field and produce secondary scintillation photons. The signal generated by them is the so-called "S2" signal. The light of both signals is converted by the PMTs into photoelectrons (PEs), which correspond to the number of photons that are detected and are a measure of the deposited energy. Both signals can be distinguished by their widths, as S1 signals take place over a time scale of less than 150 ns, while S2 signals have a duration at the order of $\mathcal{O}(1\,\mu s)$ [28, section 3.3.10].

Using the time difference between the S2 and S1 signal, the z-position, at which the interaction happened, can be reconstructed. The hit pattern of the top array PMTs which have seen the S2 signal allows to infer the x-y-coordinates, resulting in a three-dimensional reconstruction of the interaction vertex. In addition, the size of the

S2 signal relative to the S1 signal depends on the interaction type. This allows to discriminate nuclear recoils, which WIMPs are expected to cause, against electronic recoils, which result from background particle interactions.

2.3. Data acquisition (DAQ)

To process signals generated by particle interactions, waveforms of all 242 PMTs are amplified by a factor of 10 and recorded by CAEN V1724 digitizers [29], which have sampling rates of 10^8 Hz, 14-bit resoultion and a range of 2.25 V. Because these digitizers use circular buffers with 521 kB memory per channel, deadtimes are negligible for the usual background rates, which are at the order of $\mathcal{O}(1\,\text{Hz})$. Only waveform samples around baseline excursions larger than a peak height corresponding to 0.3 PE are stored. This reduces computational cost, and allows for rates at $\mathcal{O}(10\,\text{Hz})$ without deadtime.

Waveform recording is triggered, if the summed signal of a fixed set of 16 PMTs from the bottom array and the 68 inner PMTs of the top array exceeds a certain threshold. The threshold is set such, that the trigger efficiency for S2 signals larger than 150 PE is $> 99\,\%$. To not lose any information, regardless of whether an S2 or an S1 signal causes a trigger, the event window is centered on the triggering signal and chosen to have a length of 400 µs, which is twice the maximum electron drift time (176 µs at 0.53 kV/cm drift field).

2.4. Radon distillation test setup

For probing distillation as a possible method for separating radon from xenon, a packed distillation column, designed and manufactured to separate krypton from xenon in XENON1T [30], is connected to the XENON100 detector via an additional gas system and being operated in reverse mode. An illustration of the setup can be seen in figure 2.3. Xenon coming from the XENON100 detector is enriched with ^{222}Rn by flushing it through a radon source. The source consists of 426 Viton O-rings, for which estimates with large systematic errors give a rough emanation estimate of 70 mBq of ^{222}Rn [31, 32].

After having passed the source, the xenon flows into the aforementioned distillation column. Inside of it (figure 2.4) [30], at the bottom of the column, is a reservoir,

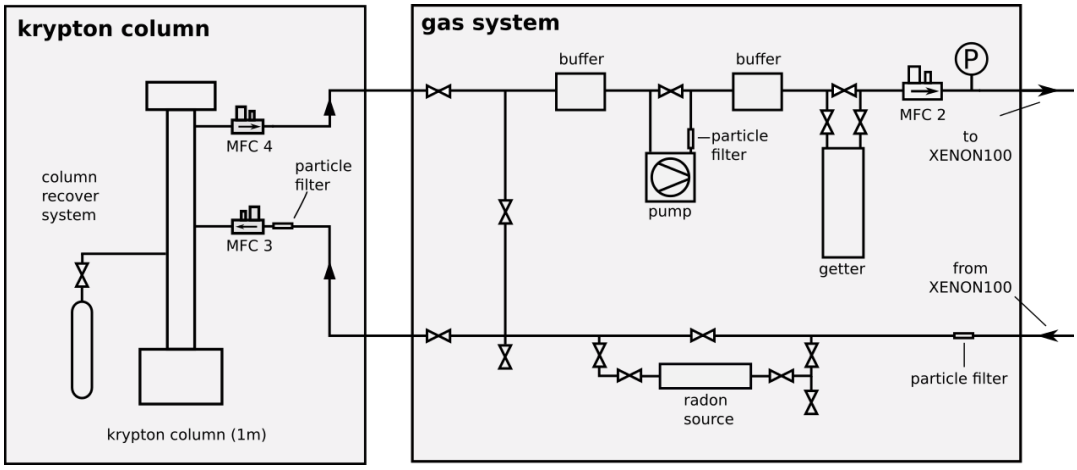

Figure 2.3.: Diagram of the radon distillation test setup [31], which is described in the text.

the so-called "reboiler" (figure 2.4), which collects and boils LXe that is dropping down from above. At the top of the column, a condenser liquefies xenon again. Both together maintain a constant flow of GXe and LXe across the column [30]. When comparing the boiling point at atmospheric pressure of radon ($T_\mathrm{b} = -61.7\,°\mathrm{C}$ [18]) to that of xenon ($T_\mathrm{b} = -108.9\,°\mathrm{C}$ [18]), radon is expected to concentrate in the reboiler, while the xenon in the top region of the column is radon-depleted [31, 32]. This radon-depleted xenon is then extracted from the distillation column via the help of a recirculation pump, which pumps the xenon back into the XENON100 detector. Normally, the concentration of radon inside the reboiler would reach a saturation limit. As radon, however, decays after a while, the column's ability to bind radon replenishes with time [31, 32].

To test the effectiveness of distillation, the following procedure is carried out: Xenon is flushed through the radon source while bypassing the column, until the radon concentration level inside XENON100 has stabilized. Then, the radon-enriched xenon is passed through the distillation column before being fed back into the detector, while xenon coming from the detector is still flushed through the source. At all times, the radon concentration inside XENON100 is monitored by analyzing datasets, which are taken during a distillation run, to look for events of the ^{222}Rn decay chain. The next chapter provides an example for such an analysis.

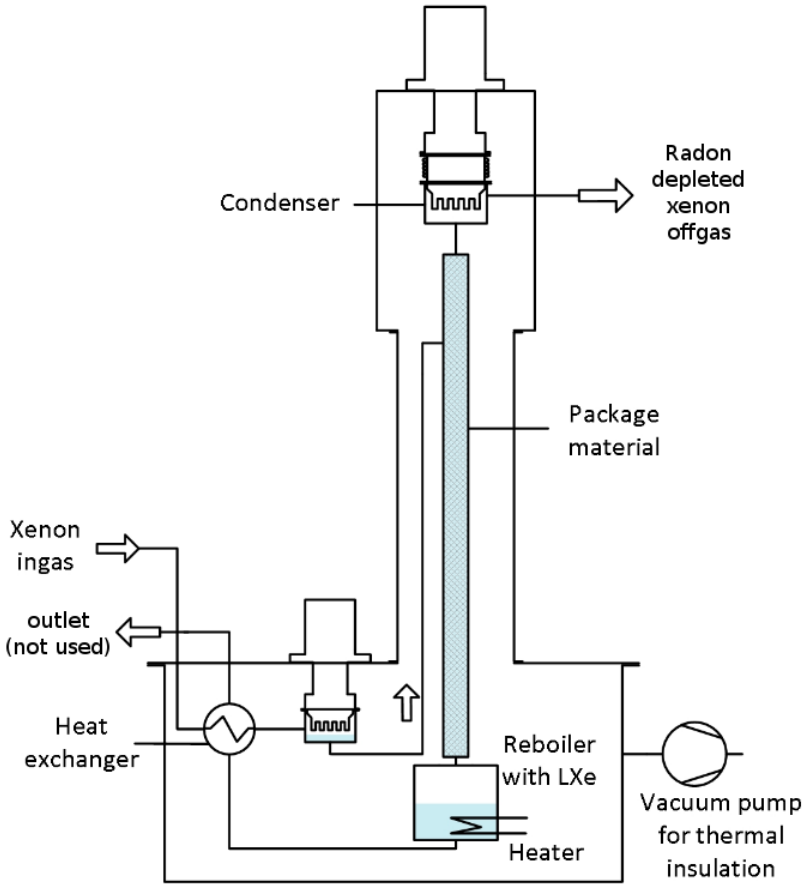

Figure 2.4.: Schematic of the distillation column which is used for the radon distillation test (illustration taken from [30] and modified). The package material provides a large surface for xenon to condense and evaporate at.

3. Identifying ^{222}Rn decay chain events in XENON100

In this chapter, an analysis for selecting ^{214}Po events is outlined. It utilizes the fact, that the α-decay of ^{214}Po, due to its short half-life of $T_{1/2} = 162.3\,\mu s$ [23], happens in such a short amount of time after the β-decay of its mother nuclide, ^{214}Bi, that signals of both are present within the same recorded waveform. These events are called bismuth polonium (BiPo) events, and possess a clear signature according to which they can be selected for. The goal of this analysis is to determine the reduction of the ^{222}Rn concentration inside XENON100 during a radon distillation test (also called "radon distillation run" from now on) by estimating ^{218}Po event rates.

The analysis is based on the BiPo analysis done in [22, chapter 4], which uses data from a XENON100 science run [16]. As several detector parameters (noise, electric field configuration) were different during the radon distillation run compared to the aforementioned science run, selection cuts need to be re-evaluated and motivated anew. Furthermore, several details of the analysis are re-worked. For cross-checks, the analysis is also applied to the science run dataset used in [22, chapter 4], with different run conditions being accounted for.

3.1. Estimating event rates of the bismuth polonium (BiPo) coincidence

As mentioned before, BiPo events contain S1 signals of both decays within a single waveform (figure 3.1). As α-particles have a larger energy loss per unit length compared to electrons at similar kinetic energies due to having more charge and mass, the ionization tracks they produce are denser. This leads to a higher probability for ionization electrons to recombine, causing a larger S1-to-S2 ratio compared to electrons, which has been verified by previous XENON100 ^{222}Rn studies [32]. Because the ^{214}Po α-decay is monoenergetic and has a larger Q-value than the ^{214}Bi β-decay

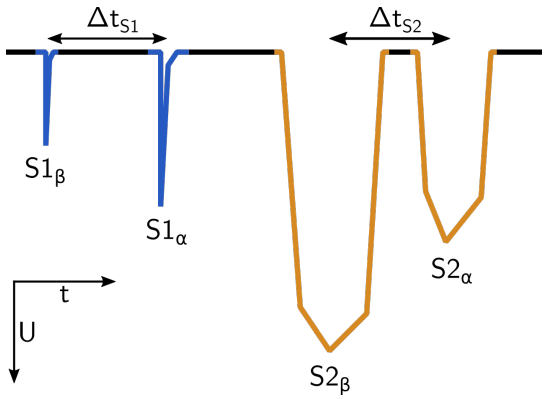

Figure 3.1.: Idealized schematic of a BiPo event candidate waveform. Both S1 and S2 signals of both decays are visible, with the earlier S1 being smaller than the one that follows it.

(7.83 MeV compared to 3.27 MeV [23]), the ^{214}Po decay's S1 (called "$S1_\alpha$" from now on) is consequently guaranteed to be larger than the S1 of the ^{214}Bi decay (called "$S1_\beta$" in the following). An exception to this might be extreme cases like events happening directly at the TPC walls or at other obstructions, which causes parts of the S1 signals to be lost. However, as the ^{214}Po half-life is short, causing it to decay at its initial position, it is unlikely, that $S1_\alpha$ is affected by a loss in signal, while $S1_\beta$, at the same time, is not. Thus, the very basic BiPo event signature consists of a real, physical S1 signal being followed by a larger one. "Real", in this context, means, that more than one PMT has seen at least 0.35 PE each, ruling out dark pulses and other kinds of signals only seen by a single PMT.

One needs to take other events into account which exhibit the same signature. ^{220}Rn, similar to ^{222}Rn, is produced by trace amounts of its mother nuclides (^{228}Th and ^{232}Th in this case) within detector materials, and is emanated into the detector volume. The ^{220}Rn chain also has a BiPo coincidence, consisting of the decays of ^{212}Bi and ^{212}Po. Because ^{212}Po has a much shorter half-life than ^{214}Po (300 ns compared to 162.3 µs [23]), about 99.9 % of these unwanted events can be cut out by requiring, that $S1_\alpha$ occurs at least 2 µs after $S1_\beta$.

Another requirement for the two S1 signals is, that they have to be larger than 200 PE each. The reason for this is to cut out noise pulses identified as S1 signals by the peak finder, which, due to multiple PMTs being noisy, might also be "seen" by more than one PMT. For S1β, only a small part should be removed by the above requirement, as, due to the Q-value of the decay being at $\mathcal{O}(3\,\text{MeV})$, larger signal sizes are expected

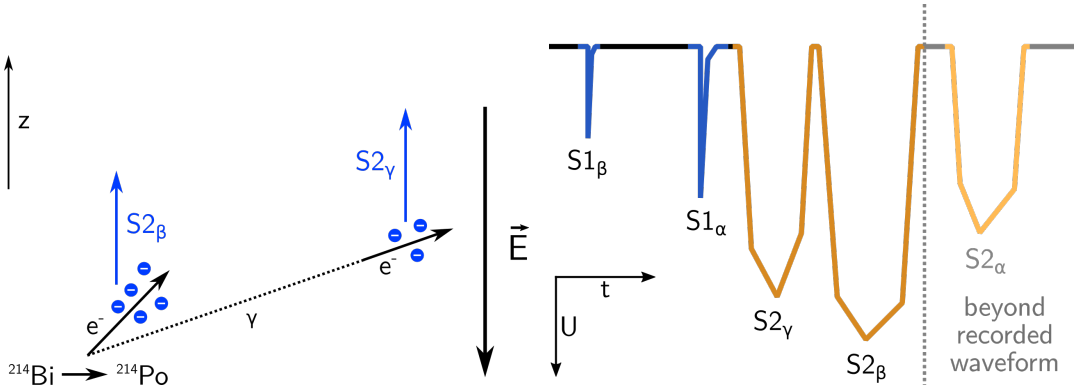

Figure 3.2.: (Left) Schematic of a gamma photon emitted directly after the ^{214}Bi decay causing an additional S2 signal. (Right) Illustration of how the idealized BiPo signature can be altered.

on average. As α-particles typically generate S1s at the order of $\mathcal{O}(10^5\,\mathrm{PE})$ [32], the effect on $\mathrm{S1}_\alpha$-acceptance is effectively non-existant.

The first set of event selection cuts is then:

- The event contains at least two peaks identified as S1.
- Both are larger than 200 PE.
- For both, at least 0.35 PE of their signal is seen by at least two PMTs.
- The largest S1 signal follows the second-largest S1 signal after at least 2 µs.

No requirements are made for S2 signals, despite the fact, that there is seemingly no reason for them to be absent at first glance. There are three major reasons for this: First, the amount of generated S2 signals might be larger than two, as ^{214}Bi does not directly decay into the ground state of ^{214}Po in 20.33 % of cases [23]. This causes γ radiation photons to be emitted during the de-excitation of the daughter nucleus. The S1 signal generated by aforementioned photons interacting with LXe happens, on the timescale of the waveform digitizer (100 MHz) at the same time as the S1 signal generated by the decay electron, so both get added up. However, as the photons are able to travel away from the location of the decay before interacting again, they might interact with LXe at a different vertex (figure 3.2, left). This causes an additional S2 to be created (figure 3.2, right).

Second, $\mathrm{S2}_\alpha$, the S2 belonging to the ^{214}Po decay, might not be recorded within the same waveform as the S1 signals (figure 3.2, right). This happens for events, in which

^{214}Po is decaying too late for the $S2_{\alpha}$ ionization electrons to arrive at the anode before the end of the waveform. For radon distillation data, the recorded waveforms have a length of 480 µs, with the triggering signal being positioned in the middle at approximately 240 µs. As the maximum expected drift time under radon distillation conditions is about 194 µs (reduced drift field compared to science runs), it is possible for the S2 signal of an $S1_{\alpha}$ to be missed if $S1_{\alpha}$ occurs between 46 µs and 240 µs after the triggering signal. In the case of $S1_{\beta}$ being the triggering signal, which is very often the case due to the large decay energy of ^{214}Bi, this corresponds to a fraction of roughly:

$$\int_{46\,\mu s}^{240\,\mu s} \frac{T_{1/2}(^{214}\mathrm{Po})}{\log(2)}\, 2^{\frac{-t}{T_{1/2}(^{214}\mathrm{Po})}} \mathrm{d}t = 2^{\frac{-46\,\mu s}{T_{1/2}(^{214}\mathrm{Po})}} - 2^{\frac{-240\,\mu s}{T_{1/2}(^{214}\mathrm{Po})}}$$

$$\approx 0.08$$

^{214}Po decays. For the usual drift field with which the science run data was taken, the values are similar.

Third, it has been found out in [22, section 4.6], that many BiPo events happen, due to ion drift effects, at or below the cathode, where the charge generated by the decay might drift towards the screening mesh protecting the bottom PMT array. If this happens, no S2 signals are produced.

However, S2s are still important in other regards. Because XENON Raw Data Processor (xerawdp), the data processor for XENON100, has been optimized for finding single scatter signals, which is what one would expect from a WIMP interaction, its peak finder stops searching for S1 signals after an S2 signal matching at least one of the following criteria has been met [28, section 3.4.3] [22, section 4.4.2]:

- It is the largest S2 in the waveform in terms of area.
- Its height is larger than 50 mV.

This limits the window within which S1 signals can be found after the inital $S1_{\beta}$. To be able to correct for this later on, the time difference between $S1_{\beta}$ and the S2 closest to it which meets the above requirements is calculated by examining all identified S2 peaks. In the following, this acceptance time window is called $T_{\mathrm{win.}}$. As the height variable used internally by xerawdp is not the same as the one saved in its output, due to them being extracted out of different kinds of waveforms, the height criterion had to be set more conservatively. Based on the plot in figure 3.3, left, a voltage of 450 mV has been chosen, as no S1 peaks were found to occur after any S2 which

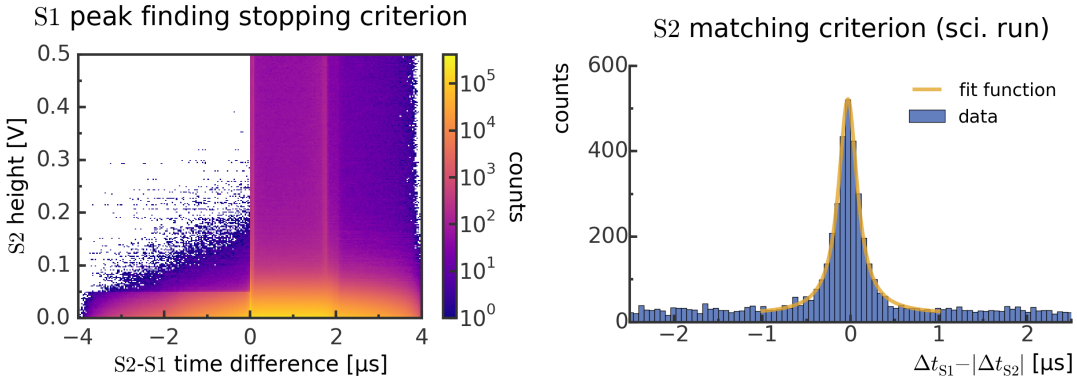

Figure 3.3.: (Left) S2 height versus S2-S1 time difference for all possible S2-S1 pairs, with negative values indicating an S1 having happened after an S2. The threshold used internally by xerawdp (50 mV) is found to be smeared out. (Right) Difference between Δt_{S1} and $|\Delta t_{S2}|$, which should be close to 0 if both pairs belong to a BiPo event.

has this height. If an event does not contain any S2 peaks, $T_{\text{win.}}$ is set to the time difference between the position of $S1_\beta$ and the end of the waveform.

S2s are also necessary for determining the position of an interaction, for which it is imperative to correctly map them to their corresponding S1 signals. Because the number of S2 signals varies for reasons mentioned before, this task is not trivial. However, as ^{214}Po is expected to decay at the same location as its mother nuclide due to its short half-life, the time difference between the S1 signals of the two decays should be the same as the time difference between their S2 signals. Thus, if an S2 pair with a similar time difference than that between $S1_\alpha$ and $S1_\beta$ can be found, it is very likely, that they indeed belong to the same decays. To devise a criterion for matching an S2 pair to the initial $S1_\alpha$- $S1_\beta$ pair, the distribution of the difference between the S1 pair time difference (Δt_{S1}) and the absolute value of the S2 pair time difference (Δt_{S2}) for all possible S2 pairs is examined. Only events which meet the previously mentioned S1 selection cuts and contain at least two S2 peaks are considered. Furthermore, only S2 peaks which are larger than 500 PE are taken into account to avoid using S2 signals which are smaller than expected. Visible within this distribution (figure 3.3, right) is a peak close to 0, which is described well by a sum of a Lorentz distribution and a constant (p-values of at least 0.25 for both fits):

$$f(x) := N \frac{1}{1 + (\frac{x-\mu}{\sigma})^2} + C \tag{3.1}$$

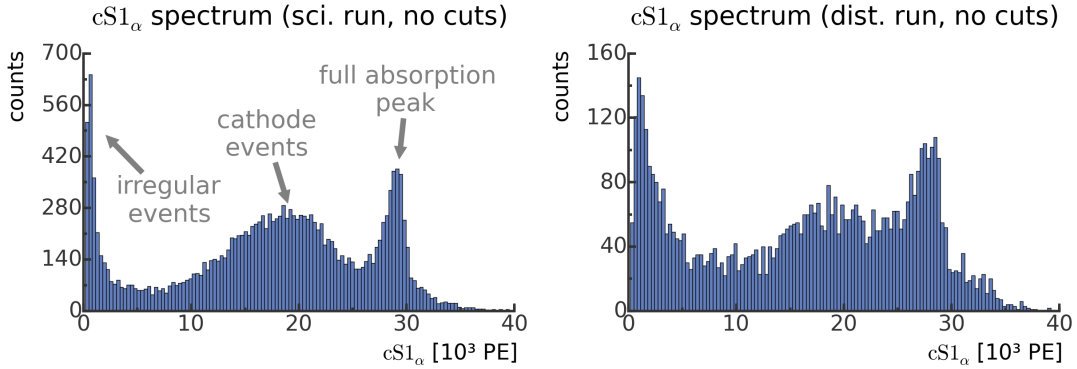

Figure 3.4.: Pure cS1$_\alpha$ spectra of both datasets. Besides the first set of selection cuts to identify possible BiPo, no additional cuts have been applied.

Because the science run dataset provides more statistics compared to the radon distillation dataset and the parameters of both fit results were found to be compatible with each other, the former's best fit parameters are taken for defining the following procedure for S2 peak matching:

- Consider only S2s larger than 500 PE as "valid".
- If the event has at least two valid S2 signals, look at all possible valid S2 pairs. If $|\Delta t_{\mathrm{S1}} - |\Delta t_{\mathrm{S2}}| + 30\,\mathrm{ns}| < 820\,\mathrm{ns}$, a match is assumed. The earlier S2 peak is assigned to S1$_\beta$, while the later one is assigned to S1$_\alpha$ instead. If multiple valid S2 pairs match the time difference criterion, the pair with the largest combined S2 size is chosen.
- If either only one valid S2 peak exists or no time difference match has been found, assign the largest S2 peak to S1$_\beta$.
- If no valid S2 exists, assume, that the decays happened at or below the cathode, and assign the minimum possible height to them ($z_{\mathrm{min.}} = -303.56\,\mathrm{mm}$, [32]).

After S2 matching, event parameters like S1/S2 sizes etc. have to be corrected, as they depend on the location of the interaction they belong to as well as on the particle causing them. For events containing no valid S2 signal, for which consequently no information about the x and y coordinates exists, the correction factor's averages at $z_{\mathrm{min.}}$ are applied to have an at least rudimental correction. The averages are determined by a parameter scan over the entire TPC area at $z_{\mathrm{min.}}$. Corrected quantities are prefixed with "c" in the rest of this chapter to distinguish them from uncorrected ones.

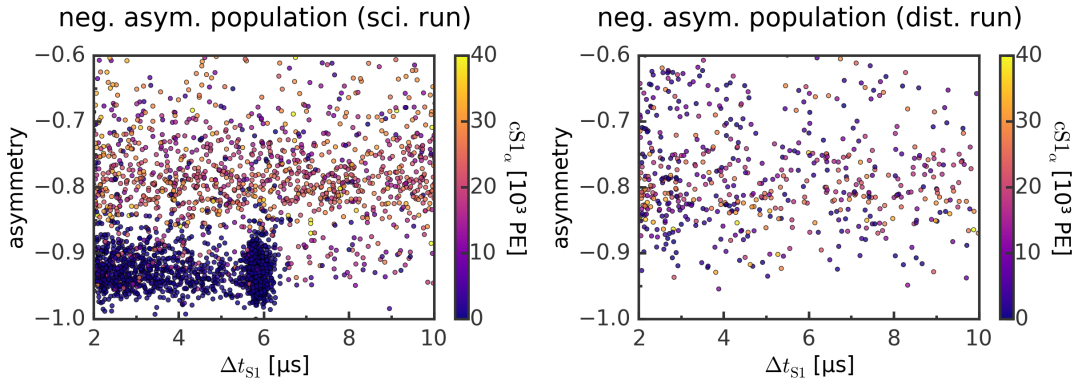

Figure 3.5.: Asymmetry versus Δt_{S1} scatter plots for both datasets. Brighter points indicate larger $cS1_\alpha$ values.

At this point, one is able to have a first look at the $cS1_\alpha$ and $cS1_\beta$ spectra. Both the science run and the radon distillation run spectra (figure 3.4) exhibit the same features, i.e. a full absorption peak as well as a more diffuse peak of events with reduced signal sizes due to be located at the cathode (already seen in [22, chapter 4]). However, an additional, irregular population of low $cS1_\alpha$ is unexpectedly visible, which necessitates additional selection cuts.

Investigation of the science run data shows, that the low cS1 population consists of $S1_\alpha$ peaks seen almost exclusively by the bottom PMT array. This "asymmetry" is quantified as follows:

$$asym := \frac{S1_{\text{top}} - S1_{\text{bot.}}}{S1}, \tag{3.2}$$

with $S1_{\text{top}}$ referring to the part of the signal seen by the top PMT array, while $S1_{\text{bot.}}$ likewise refers to the part seen by the bottom one. Interestingly, these events all happen to have $\Delta t_{S1} < 7\,\mu s$ (figure 3.5,left), so a more restrictive version of the S1 selection time cut, i.e. requiring $\Delta t_{S1} > 7\,\mu s$, gets rid of them. The population is not visible in radon distillation data (figure 3.5, right).

Because of edge effects at the TPC walls and the anode/cathode, position cuts need also to be looked at. As the spectrum of events reconstructed outside the TPC exhibits the same features as that of events reconstructed within (figure 3.6, left), a cut on an event's radius relative to the center of the TPC (R) is not applied to retain acceptance. However, it is required, that the z coordinate is larger than $z_{\text{min.}}$, as it cannot be assumed, that the signal correction maps are still well-defined at unphysical coordinates. The amount of events removed by this cut is negligible, so no argument against it like in the case of a radial cut can be made. Of course, this also means,

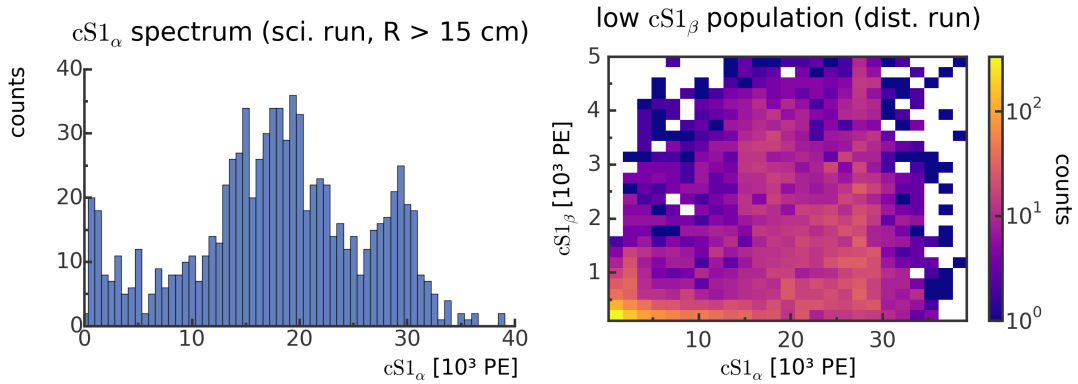

Figure 3.6.: (Left) Science run $cS1_\alpha$ spectrum of events which would have been cut, if one would require events to be within a radius of 15 cm to the TPC's center (the diameter of the TPC is 30.6 cm [1]). (Right) $cS1_\beta$ versus $cS1_\alpha$ for distillation run data. Note the extreme concentration of events at low S1 sizes.

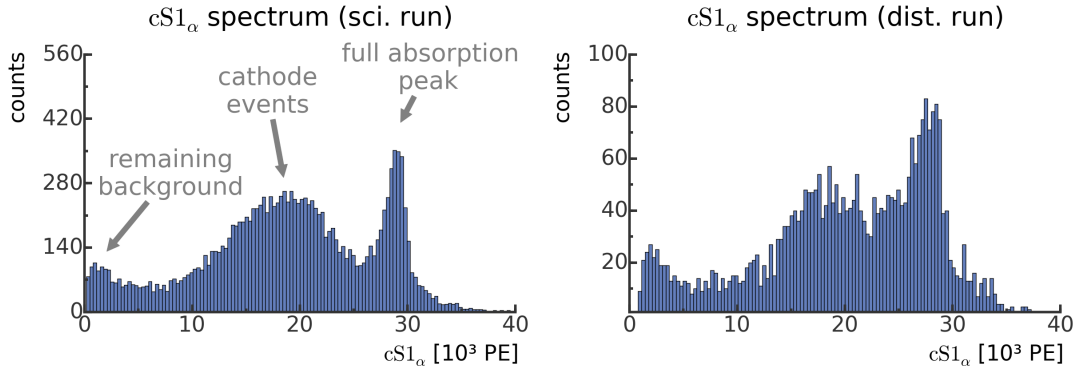

Figure 3.7.: $cS1_\alpha$ spectra of both datasets after having applied the second set of selection cuts.

that such an argument would be unnecessary due to the cut's minimal influence.

In the radon distillation dataset, the low $cS1_\alpha$ population is caused by a different effect than the one causing the low $cS1_\alpha$ population in the science run dataset. This is evident considering the fact, that no negative asymmetry population is observed in the radon distillation data as previously mentioned. Instead, it correlates with low $cS1_\beta$ values (figure 3.6, right) and does not distinguish itself otherwise. Consequently, only a requirement on $cS1_\beta$ is able to remove it, reducing BiPo acceptance in the process.

In summary, the second set of event selection cuts is:

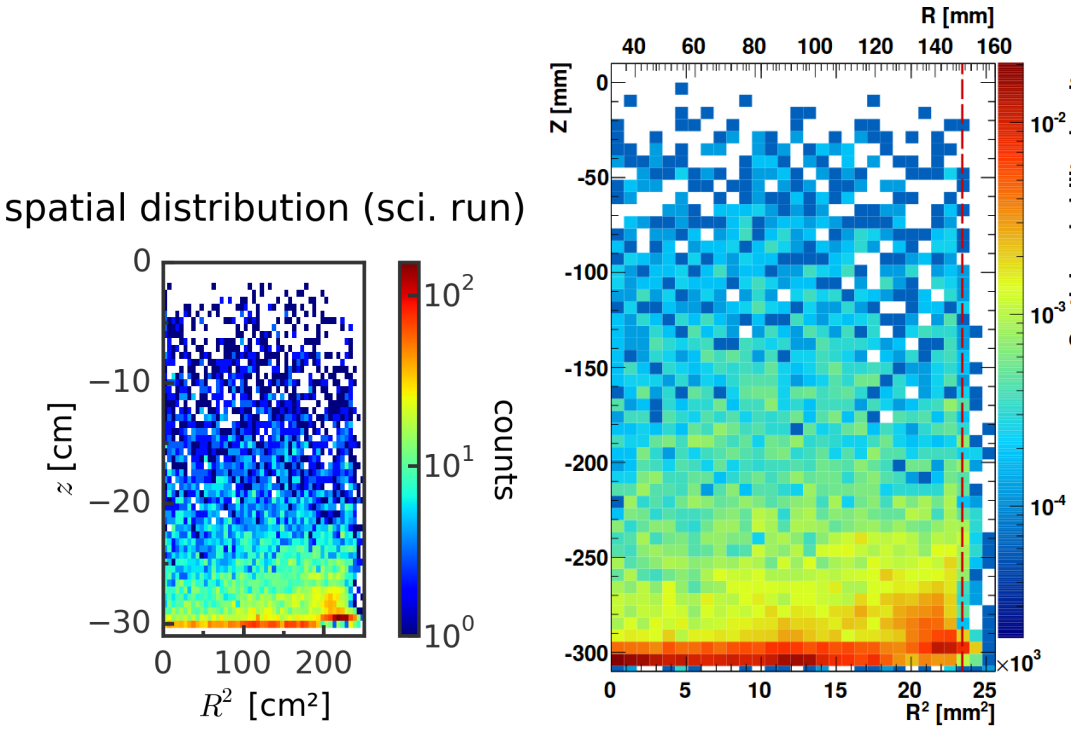

Figure 3.8.: (Left) Spatial distribution from this analysis. (Right) Spatial distribution from [22, section 4.6.3].

- The largest S1 signal follows the second-largest S1 signal after at least 7 µs (applied to both datasets).
- The reconstructed z coordinate must be larger than or equal to $z_{\text{min.}}$ (applied to both datasets).
- cS1_β must be larger than 750 PE (applied to the radon distillation dataset only).

After applying these, the irregular population of low cS1_α events disappears at large, but a part of it still remains (figure 3.7).

Using the extracted position information from events which contain at least one valid S2 signal, one can now compare the spatial distribution of BiPo event candidates in the science run dataset with the one given by [22, section 4.6.3] (figure 3.8). In both plots, the same basic features are visible. Especially notable is the concentration of BiPo event candidates around $z_{\text{min.}}$, which is at the cathode. Furthermore, the total number of BiPo event candidates in the science run dataset, which amounts to 14900, is at the same order of magnitude as the number stated in [22, section 4.4.2], which is 16500. To now be finally able to give a ^{214}Po rate estimate, the acceptance loss

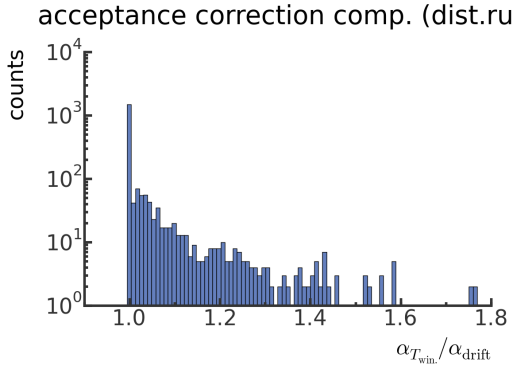

Figure 3.9.: Comparison of the correction factor α obtained by using $T_{\text{win.}}$ to the one obtained by using the drift time.

due to the behavior of xerawdp's peak finder has to be taken into account. This is achieved by weighting each event with the inverse of the acceptance defined by the time window $T_{\text{win.}}$, which is, after integrating over the corresponding bounds of the exponential decay distribution:

$$\begin{aligned}\alpha &= \left(\int_{7\,\mu\text{s}}^{T_{\text{win.}}} \frac{T_{1/2}(^{214}\text{Po})}{\log(2)}\, 2^{\frac{-t}{T_{1/2}(^{214}\text{Po})}}\, \mathrm{d}t \right)^{-1} \\ &= \left(2^{\frac{-7\,\mu\text{s}}{T_{1/2}(^{214}\text{Po})}} - 2^{\frac{-T_{\text{win.}}}{T_{1/2}(^{214}\text{Po})}} \right)^{-1}, \end{aligned} \tag{3.3}$$

when taking into account, that Δt_{S1} has to be larger than 7 µs as it is required by the cuts. The old analysis used the time difference between S2_β and S1_β, i.e. the drift time, instead of $T_{\text{win.}}$, implicitly assuming, that it is unlikely for an S2 causing the peak finder to stop looking for S1 signals to appear between them. Considering possible additional S2 signals due to γ radiation photons, as it has been described before, this assumption is questionable. Directly comparing the event weights obtained by both approaches (figure 3.9) shows, that the weights obtained by using $T_{\text{win.}}$, as in this analysis, are, on average, about 4 % larger compared to those obtained by using the drift time, indicating a moderate effect on the event rate correction.

The result for a period of the science run, where data about ^{222}Rn and ^{218}Po is available, is shown in figure 3.10, left, with the ^{222}Rn and ^{218}Po rates taken from a previous analysis which specifically examined this kind of events during the given timeframe [32]. By taking the ratios of the ^{214}Po rate to the other components and fitting a constant to their evolution, one sees, that they can be assumed to

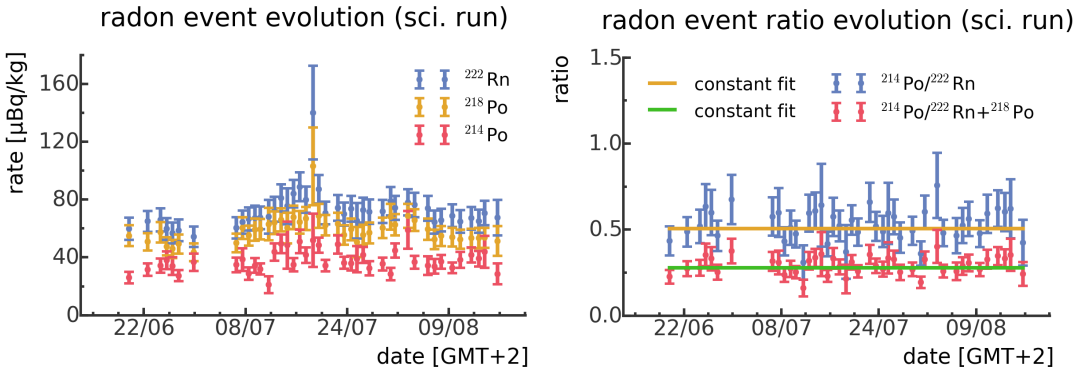

Figure 3.10.: (Left) ^{222}Rn event rate evolution during the science run. Red data points are from this analysis. (Right) Evolution of ratios between the estimated ^{214}Po rate and other ^{222}Rn event rates.

be constant (p-values larger than 0.5). The ratio between ^{214}Po and ^{222}Rn, which has been estimated to be $(50.7 \pm 1.5)\,\%$, is compatible with the ratio given in [22, section 4.7], which is approximately 50 %. As the rates shown in the evolution plot do not fluctuate much, nothing can be inferred about a possible, constant background contribution, which would manifest as a change in event ratios depending on how high event rates are.

At the end, the analysis presented in this section has shown to be consistent with the old one, which, due to similar methodology, should not come as a surprise. Nonetheless, improvements, like a more accurate computation of time acceptance corrections, could be made. Also, it was found, that almost the same cuts can be applied to the radon distillation dataset, with only an additional cut on $\mathrm{cS1}_\beta$ being necessary.

3.2. Quantifying the reduction in ^{222}Rn achieved by distillation

One is now finally able to look at the ^{214}Po rate evolution during the radon distillation run mentioned in the chapter's introduction. The combined rates of ^{222}Rn and ^{218}Po events are taken from an analysis done by [31].

Looking at the rate evolution plot, a clear correlation between both rates is visible. Also, the points, at which the ^{222}Rn source was opened and where operation of the column started are clearly visible. The spatial distribution plots show (figure 3.11, right), that BiPo events are still concentrated near the cathode, but not as much as

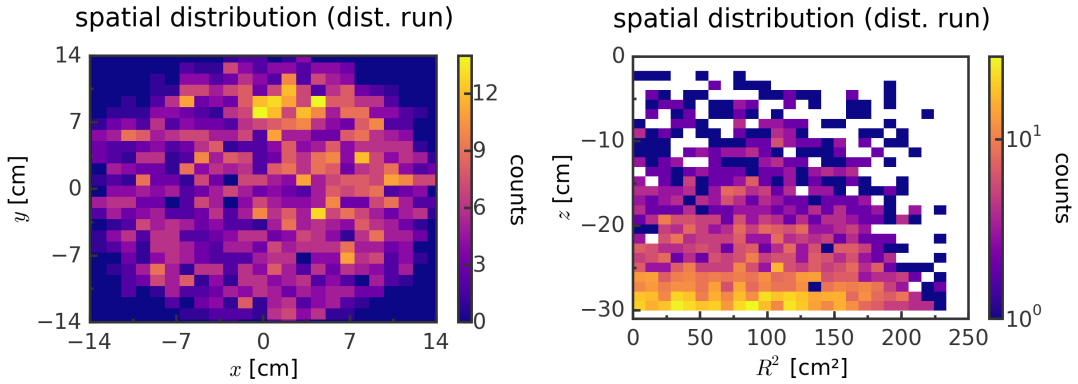

Figure 3.11.: Spatial distribution of BiPo event candidates in the distillation run dataset.

during the science run. This can be explained by ^{214}Bi remaining ionized after being produced, which makes it subject to the drift field inside the TPC, as it has been found out in [22, section 4.6] as previously mentioned. Due to the drift field having been smaller as usual during the radon distillation run, the ionized ^{214}Bi decays before reaching the cathode more often. Furthermore, an excess of events in the upper right quadrant of the detector's x-y plane (figure 3.11, left) is visible, which is assumed to be background from an YBe source having been near the detector during the distillation run due to other detector studies being made. As fitting a constant to the ratio evolution still gives an acceptable fit (figure 3.12, left; p-value of about 0.09), especially considering the change in rates by two orders of magnitude during the run, there should be no major influence of background which does not correlate with the ^{222}Rn rate, to which the YBe source belongs to. A systematic deviation of parts of the data towards values larger than the constant of the fit is still apparent, however. Due to the S1 light yield being dependent on the strength of the drift field, the ratios extracted from the radon distillation run can, unfortunately, not be easily compared with the ratios from the science run. This would be even then the case, if the $cS1_\beta$ cut was applied on the science run data as well.

To now quantify the reduction in ^{222}Rn, a reduction factor, defined as the ratio between the upper rate plateau before starting distillation and the lower rate plateau during distillation, is computed. A constant is fitted to the available points at the upper rate plateau as well as all data points at the lower rate plateau[1] to obtain the average rate before starting distillation and after. The resulting reduction factor,

[1]The lower plateau is defined as starting at the beginning of stable phase of the ^{222}Rn + ^{218}Po rate and ending, when the ^{222}Rn source used for the distillation run was closed.

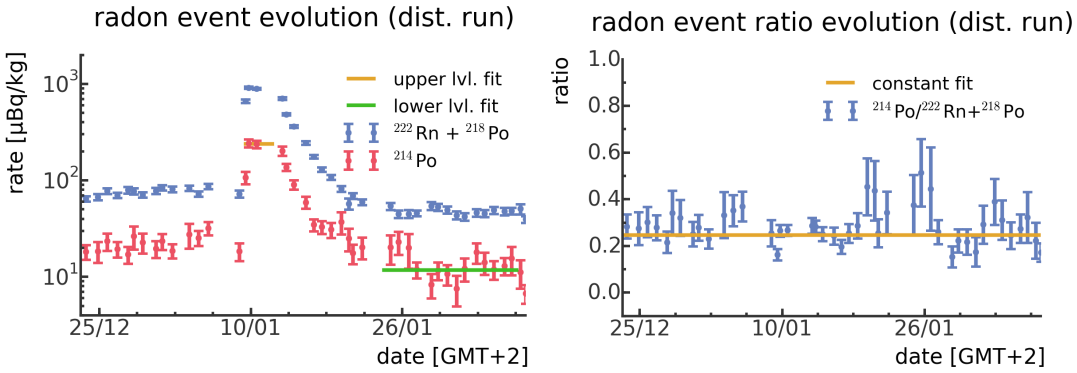

Figure 3.12.: (Left) ^{222}Rn event rate evolution during the distillation run. (Right) Evolution of ratios between the estimated ^{214}Po rate and the ^{222}Rn + ^{218}Po rate obtained by [31].

when only taking statistical errors into account, is:

$$R = 20.3 \pm 1.9,$$

which is compatible with the factor obtained by [31] using the combined ^{222}Rn and ^{218}Po rates, given as $R = 18.5 \pm 0.5$. No major systematical error contribution is expected, because R as a ratio does not depend on event acceptances. Also, it has been shown, that the ratio between the two rates which are plotted remains constant, even when both rates rise steeply. This indicates, that constant background contributions do not play a major role.

3.3. Conclusion

In this chapter, a selection procedure for BiPo event is devised. In parallel, measures are taken to correct for acceptance losses, which happen due to the behavior of xerawdp. Also, a method for matching S2 peaks to BiPo S1 peaks is provided in order to extract an event's position information.

The selection procedure is seen to not remove all background events. However, as it can be seen in the ratio plots, ratios between decay rates from the ^{222}Rn chain remain constant even with the rates changing over two orders of magnitude. This signifies, that no major constant background source is to be expected.

At the end, this analysis passed a cross-check with a previous BiPo analysis [22, chapter

4] and was successfully applied to quantify the effectiveness of the distillation column which has been used. The reduction in radon concentration has been determined to be:

$$R = 20.3 \pm 1.9,$$

which is compatible with a value of $R = 18.5 \pm 0.5$ determined by [31]. Consequently, the separation of radon from xenon via a distillation column has been shown to work.

4. The HeidelbergXenon (HeXe) system

In order to study ^{222}Rn decay chain events in LXe in more detail compared to XENON100 as well as to conduct general detector research and development, a multipurpose xenon system, called HeXe, has been built at the Max-Planck-Institut für Kernphysik (MPIK). During its first phase, the system was used for checking the feasibility of separating radon from xenon by employing distillation techniques [25]. For its second phase, it is modified to host two PMTs, which are mounted such, that they face each other. This allows for testing these PMTs in GXe and in LXe. In addition, it is made possible to detect xenon scintillation light, generated by particle interactions, by triggering on coincident signals.

Measurements with radon-enriched xenon, described in chapter 5, have been carried out for ^{222}Rn decay chain event studies in GXe and LXe. The following sections provide a description of the entire second phase HeXe setup, which was used for these measurements.

4.1. Cryostat and main structure

The heart of the HeXe system is a double-walled, cylindrical stainless steel cryostat, with an inner diameter of 201 mm and an inner height of 540 mm. It stands on a raisable platform held by a support structure (figure 4.1). The volume between its walls is evacuable, and its inner wall contains 25 layers of multi-layer insulation, both to reduce heat input from outside. Its bottom plate may be heated up to allow for limited baking and to accelerate boiling off liquid gas, making use of an embedded 90 W heating foil and Pt100 sensor combination connected to a control circuit for temperature regulation (figure 4.2, left).

The cryostat is connected to a flange, called “main flange” from now on, which is located on top of the support structure. It is also double-walled, allowing for additional thermal insulation. Four pipes are fanning out of the main flange, with each of them

ending in a smaller flange. These sub-flanges are used for feeding through cables as well as for connecting the cryostat to the HeXe gas system (see section 4.4) and to a cold head used for gas liquefication (see section 4.2).

A cylindrical PTFE block (figure 4.2) is suspended on the main flange such, that it is fitting exactly into the cryostat. The block measures 19.6 cm in diameter and 34 cm in height, while being split into two halves held together by hinges to allow for opening it. On the block's inside, holes and trenches were shaped to allow the placement of two PMTs and two optical fibers pointed towards the volume between the PMTs, which are connected to LED boards used for PMT calibration (described in section 4.5). The PMTs are held in position by copper rings and a PTFE spacer ring, with the spacer ring also acting as a diffuser surface when guiding light through the optical fibers. PMTs and spacer ring together enclose a volume of about 161 ml ($\approx$ 455 g LXe), which defines the active volume for measuremets in GXe and LXe.

On the block's outside, additional holes were shaped to hold up to eight Pt100 temperature sensors at different heights, being held in place by screws and washers (figure 4.3). Besides for monitoring temperature, these sensors also act as fluid level meters when liquefying gas inside the cryostat. As the surface of the block is very close to the raised cryostat's wall, trenches had to be drilled into the block to lead the cables of the Pt100 sensors, the lower optical fiber and the signal and power supply cables of the lower PMT towards the main flange without being squeezed. The cabling inside those trenches is held in place by screwed-on PTFE and plastic covers.

4.2. Cooling system

On top of the support structure and connected to the cryostat via the main flange, a cold head is cooled down by the expansion of helium provided by a helium compressor. It has a cooling power of 200 W and is employed for cooling down a ribbed copper block, which acts as a cold finger and provides a surface for xenon to condense at (figure 4.1, right). The xenon droplets which form on the copper block surface then drop down and are led by a funnel into the cryostat via the main flange connection. For thermal insulation, the pipe containing both cold head and copper block is double-walled, too, sharing its insulation volume with the main flange.

To control the copper block temperature, its connection to the cold head is provided by three heating cartridges mounted in-between them, which together provide up to

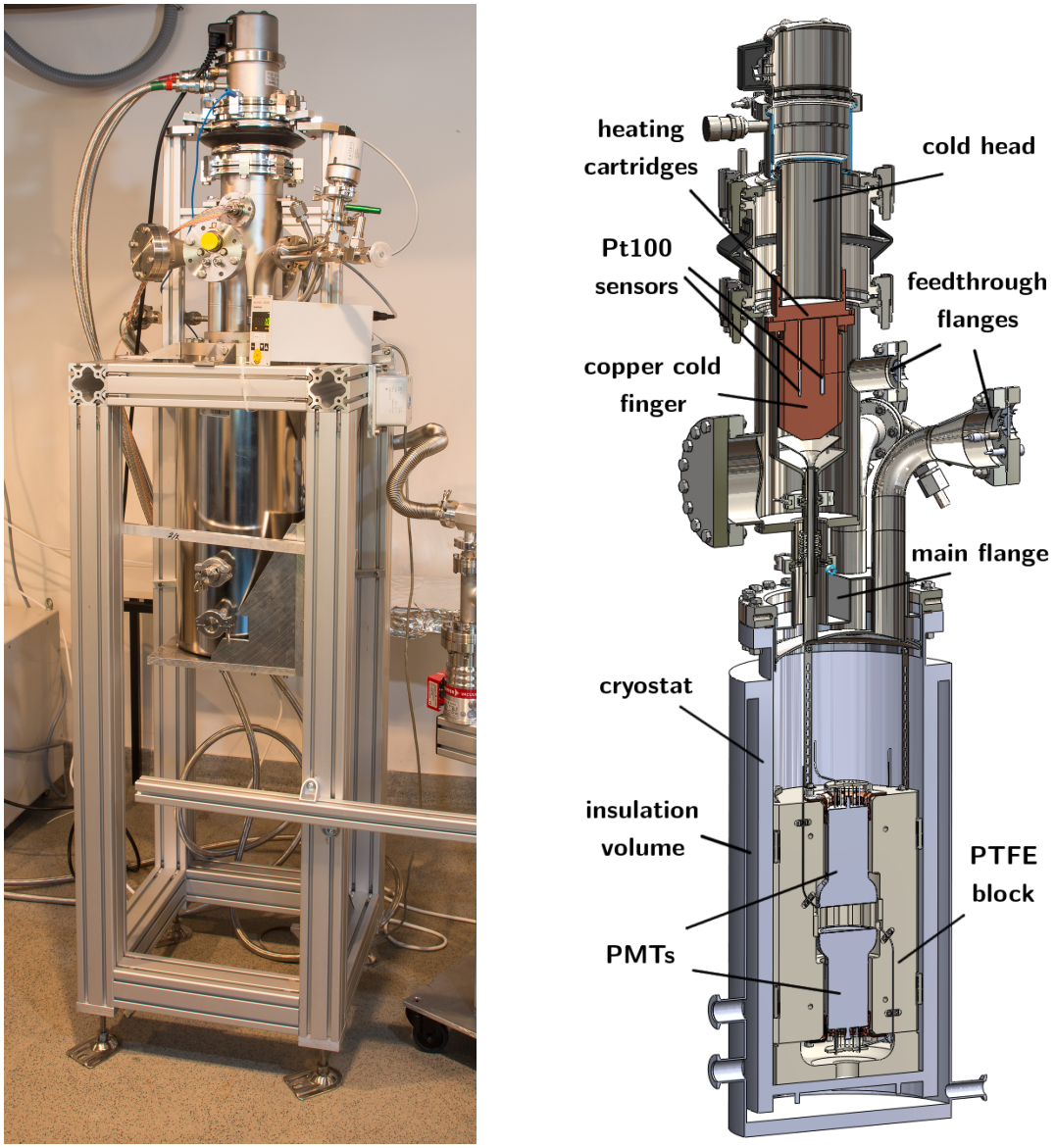

Figure 4.1.: (Left) View of the cryostat connected to the main flange. The cold head is located within the tallest pipe emerging from the main flange. (Right) Technical drawing of the view seen on the left, revealing its interior.

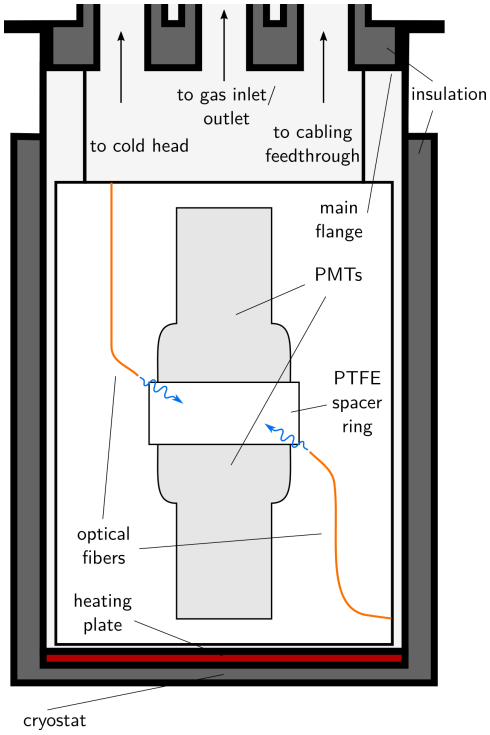

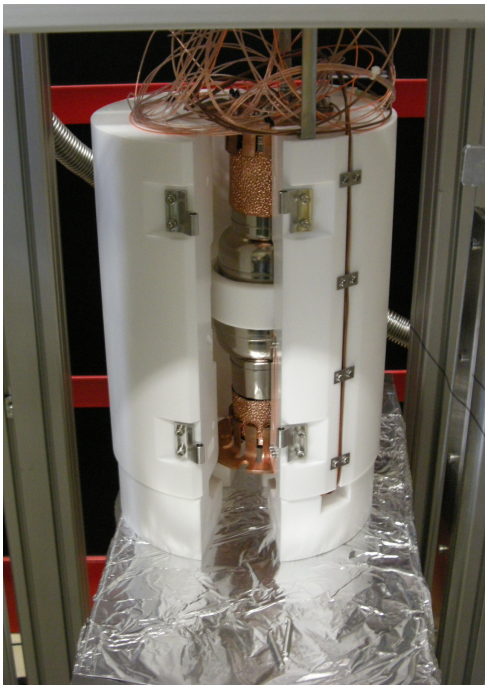

Figure 4.2.: (Left) Cross-section schematic of the closed cryostat (not to scale). (Right) View of the opened, fully equipped PTFE block.

channel	height [cm]
8	34.40 ± 0.05
7	33.00 ± 0.05
6	27.50 ± 0.05
5	22.00 ± 0.05
4	18.00 ± 0.05
3	12.50 ± 0.05
2	7.00 ± 0.05
1	3.00 ± 0.05

Figure 4.3.: (Left) View of the Pt100 sensors on the block's outside. (Right) Heights of the Pt100 sensors (relative to the block's bottom edge).

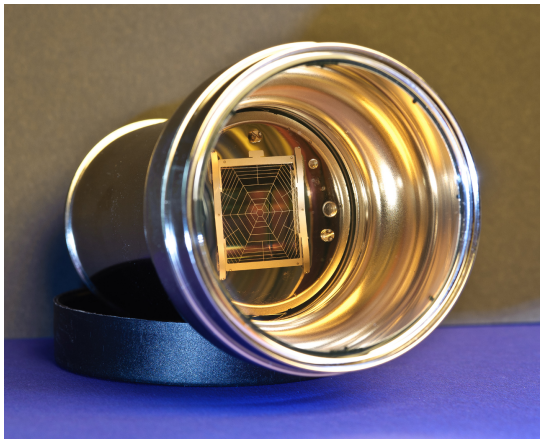

Figure 4.4.: Front view of an operational Hamamatsu R11410-10 PMT.

300 W of heating power. The cartridges are controlled by an Arduino [33], programmed to act as a PID controller, using one of five Pt100 temperature sensors embedded within the copper block for temperature feedback.

4.3. Photosensors

Two Hamamatsu R11410-10 [27] PMTs (figure 4.4) are employed for light detection, as they are specifically designed for operation in GXe and LXe. Characteristic for this PMT series are high quantum efficiency (QE) values relative to typical PMT standards (typically $> 30\,\%$) and low intrinsic radioactivity [34]. For the tubes used, the QE values are 30.6 % (top PMT) and 28.9 % (bottom PMT) respectively. They also maintain a good, stable gain (typically $\approx 3 \times 10^6$ when operated within 1.4 kV to 1.5 kV) even at temperatures around the boiling point of xenon, which, for the pressure range allowed in the cryostat, is between −90 °C and −105 °C [35, section 3.1].

4.4. Gas system

The HeXe gas system facilitates the filling of the cryostat with xenon and recuperating it after usage. Furthermore, it provides options for gas cleaning and circulation. Based on the functionality of its parts, it is divided into a source side and a recuperation side (figure 4.5).

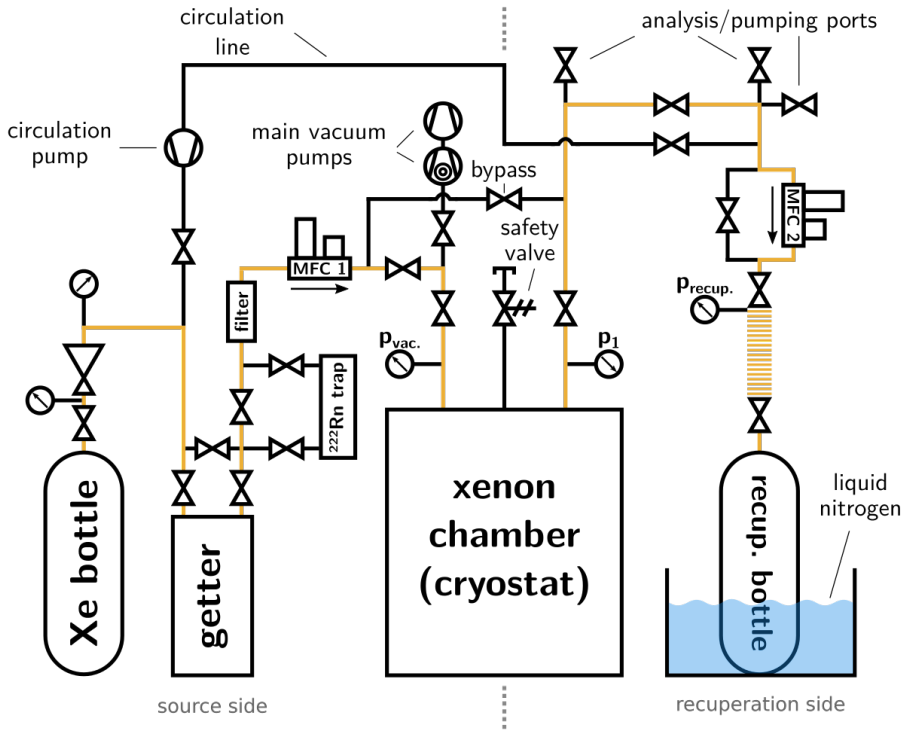

Figure 4.5.: Schematic of the HeXe gas system as described in section 4.4. The main line, which corresponds to the path usually taken by xenon used for measuring, is colored in orange.

The source side contains a xenon bottle with a mounted-on pressure regulator. When going along the main line of the gas system, the xenon leaving the bottle first passes through a getter-based purifier to reduce the amount of impurities like water and oxygen, which would limit the amount of scintillation light. Then, it may be enriched with ^{222}Rn by flushing it through a silica gel trap loaded with radon, before it flows through a particle filter, which holds back dust particles coming from aforementioned trap. Afterwards, the xenon goes directly into the cryostat, with the mass flow being monitored and controlled by a mass flow controller (MFC 1).

On the gas system's recuperation side is a gas bottle which can be immersed into a liquid nitrogen bath. This cools down the bottle to temperatures below the freezing point of xenon (which is at $\approx -112\,°\mathrm{C}$ at atmospheric pressure [18]), allowing to cryopump xenon into it. A second mass flow controller (MFC 2) controls and monitors

the mass flow into the bottle. In case of a blackout, MFC 2 can be bypassed, as it closes down when receiving no power.

There are several other components besides the main line ones. On the source side, a scroll pump connected in series with a turbomolecular pump is used for evacuating both gas system and cryostat. Several additional ports located on the recuperation side can be used for connecting additional vacuum pumps or devices for gas analysis. A bypass valve, which connects both sides, allows for bypassing the HeXe cryostat. Furthermore, the circulation line, as seen on the top-left side of figure 4.5, contains a circulation pump for leading xenon back into the getter again, enabling a more thorough purification if desired.

Finally, in order to maintain safe operation, pressure gauges are mounted at critical points of the system. Two sensors, one for sub-mbar pressures ($p_{vac.}$) and one for pressures up to 2.5 mbar (p_1), are directly connected to the cryostat for monitoring the pressure inside it during evacuation and operation with xenon. In addition, a mechanical gauge ($p_{recup.}$) is used for verifying, that a vacuum remains established during cryopumping. If the pressure inside the cryostat rises above 3.1 bar, a safety valve starts to release gas to relieve the system.

4.5. Electronics and DAQ

All PMT and Pt100 cables as well as all optical fibers are fed through a single flange. The PMT signal and Pt100 cables share a multipin feedthrough, while the PMT voltage cables and optical fibers have their own, specialized ones (SHV and FC/PC, respectively).

The PMTs are supplied via an iseg NHQ dual channel HV module [36]. Their signals are led to a Phillips Scientific 776 amplifier [37] (see figure 4.6) with a fixed gain of 10.0 ± 0.2, according to its specifications (this value is examined in section 5.2.1). From there, the amplified signals respectively go to a CAEN V1724 digitizer [29] for waveform recording (100 MHz sampling rate, 2.25 V range, 14-bit resolution), and to an N-TM 405 discriminator [38]. The discriminator is set to a trigger threshold corresponding to 1/3 of the height of a signal generated by a single-photoelectron (SPE) if the PMTs are operated at a gain of 3×10^6. This is the lowest reasonable threshold allowed by the noise conditions, as oscillations correlating with the power grid frequency of 50 Hz appear below it. For PMT pulses above this threshold, the

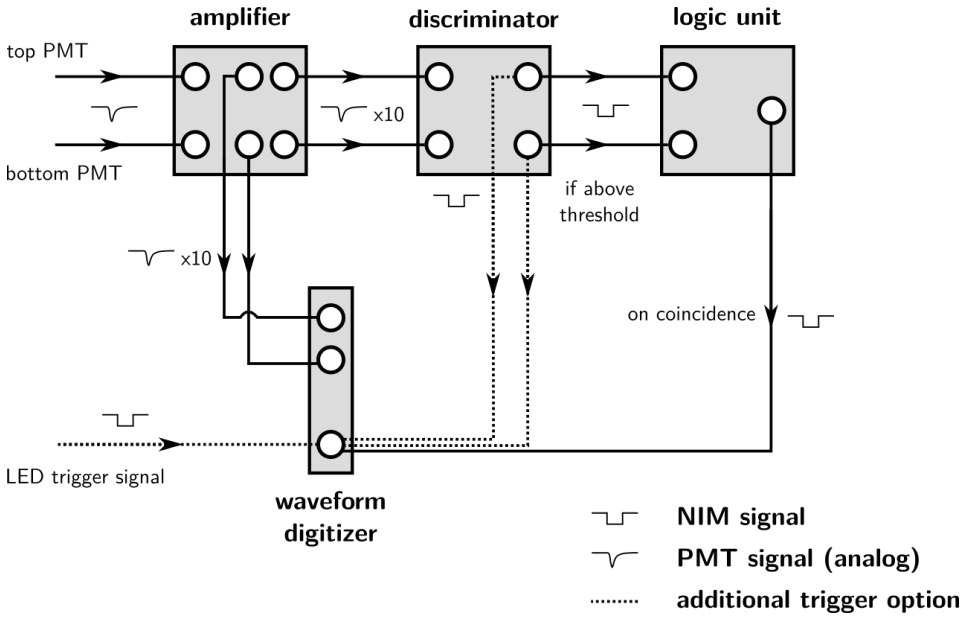

Figure 4.6.: Schematic of the signal and trigger electronics. The additional trigger options, i.e. triggering on discriminator signals from one of the PMT channels or on the LED trigger, are used for PMT characterization measurements.

discriminator is set to generate NIM signals with a width of 20 ns. These signals are sent to a logic unit which generates a 60 ns wide NIM signal, if discriminator signals from both channels are overlapping each other. The signal generated by the logic unit is then used for triggering the waveform digitizer.

DAQ is accomplished with a computer connected to the digitizer via optical link, utilizing a stripped-down version of Data Acquisition for XENON100 (DAX), the DAQ program used by XENON100 [1], for readout. This reduced DAX version is called "miniDAX". The miniDAX variant which is used for HeXe measurements stores the waveform data in the standard binary data format employed by the digitizer. Before each series of measurements, miniDAX is used to set the baseline of each digitizer channel to correspond to a sample value that ensures optimum usage of the digitizer's range. Except for LED calibration measurements (described in the next paragraph), zero length encoding (ZLE) is used to reduce the amount of disk space needed to store digitized waveforms. It works by only storing waveform samples with a value 10 samples below the baseline or lower. This corresponds to a voltage below the trigger thresholds used, so each signal large enough to cause a discriminator signal is guaranteed to have its waveform information stored. To retain information

about the baseline, 10 samples before and 100 samples after a region below the ZLE threshold are saved, too.

For calibrating the PMTs while they are inside the HeXe cryostat, LEDs with a peak wavelength of 375 nm, mounted on trigger boards, are connected to the two main flange's optical fiber feedthroughs for PMT illumination. The boards are triggered with TTL signals generated by a two-channel pulse generator, causing the LEDs to give light for a timespan of several ns. Coincident with the LED trigger pulses, the pulse generator also provides a NIM output signal, which is used for triggering the digitizer when calibrating the PMTs. By varying the source voltages applied to the LEDs, different pulse intensities can be achieved.

4.6. Slow control

The p_1 pressure sensor (see figure 4.5), one of the embedded copper cold finger temperature sensors as well as all mass flow controllers (MFCs) and PTFE block temperature sensors are read out and saved into a text file via a LabVIEW [39] program running on its own dedicated computer. The program also provides a visual interface showing the current value for each of the monitored parameters as well as automatically updating evolution plots for the p_1 and PTFE block temperature values for easier monitoring of their evolution. Basic remote monitoring is possible by using the computer's remote desktop capabilities.

The temperature sensor used for regulating the cold finger temperature as well as the currently set heating power are read out by a Raspberry Pi [40] connected to the Arduino system responsible for controlling the heater cartridges (see section 4.2). Those values are then saved into a PostgreSQL [41] database for later usage. A web interface, accessible from within the MPIK network, automatically generates evolution plots for both parameters over a certain, selectable timeframe.

5. HeXe measurements and results

In the following, the development of a processor for extracting parameters out of data taken with the HeXe system is outlined. Afterwards, the electronic components used for DAQ are characterized, which yields information necessary for the analysis of the first ^{222}Rn measurements with HeXe. Its results are described at the end of this chapter.

5.1. Low-level analysis

To process waveform data, the "walpurgisnacht" processor has been developed over the course of this thesis. At the time of writing, it offers the following features:

- Reading the binary data format employed by the CAEN V1724 waveform digitizer [29].
- General event processing, i.e. baseline estimation, peak finding and calculating event parameters like peak positions, areas etc.
- Processing serveral files in parallel via multithreading.
- ROOT TTree and ASCII output.
- Interactive event viewing by utilizing the plotting capablilties of the ROOT data analysis framework [42]. A list of event numbers may be passed to the processor to only view a certain subset of events.
- Peak finder calibration by scanning all peak finder parameters over user-definable intervals.
- Integrating waveforms over a fixed, customizable interval, which is used for PMT calibration by LED illumination.
- Generating Monte Carlo pseudo-waveforms for processor output consistency checks.

The general processing procedure consists of reading the waveform data for each PMT channel and running the peak finding and baseline estimation algorithms over them. The estimated baseline values are then subtracted from the respective channel waveform to get "baseline-corrected channel waveforms". These baseline-corrected waveforms are then added together to give summed waveforms: The "unweighted summed waveform" is calculated by summing up all channel waveforms without mutliplying them with any normalization factors. The "corrected summed waveform" instead uses such factors to normalize each channel waveform relative to a fixed amplification/gain value. These normalization factors are determined by characterizing the equipment used for DAQ (see section 5.2). After looking for peaks in the unweighted summed waveform, event parameters like peak positions, areas etc. are calculated according to the baseline-corrected channel waveforms and the corrected summed waveform respectively. At the end, these parameters are converted into SI units and, if necessary, normalized by using the aforementioned factors before storing them in the desired output format.

In the following, the processor's peak finding, baseline estimation and parameter calculation algorithms, are motivated and outlined. Also described are tests regarding the functionality of the processor.

5.1.1. Peak finding and baseline estimation

The most crucial steps of waveform data processing are proper peak finding and baseline estimation, as almost all information regarding an event is encoded within peak parameters. A good baseline estimate is needed to reliably calculate them.

Finding peaks is done by looking at differences between waveform samples. With $W[i]$ denoting the i-th waveform sample, a "difference waveform" is constructed according to:

$$W_{\text{diff.}}[i] := W[i+1] - W[i] \tag{5.1}$$

This difference waveform is then scanned, beginning at the first sample, while looking for peaks with negative polarity. Negative, because the PMTs and electronic components used for measuring produce negative polarity signals. If the difference passes a certain negative threshold (called "thr_1" from now on), denoting a possible starting flank of a peak, the peak finder stores the index of the sample where the theshold crossing happened (i_{thr_1}) and becomes active. If, and only if, a certain positive threshold (called "thr_2" from now on) is passed afterwards, signaling the possible ending

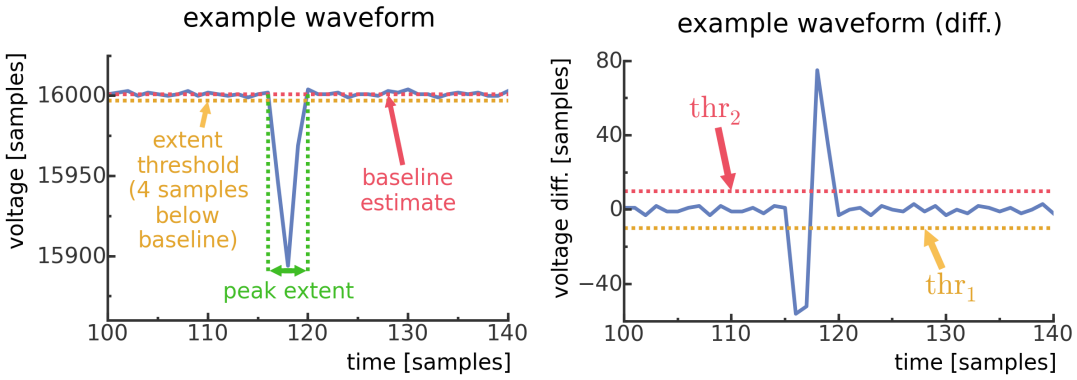

Figure 5.1.: (Left) Part of an example waveform centered on a peak, illustrating how a peak's extent is determined. (Right) Difference waveform of the example shown on the left, constructed according to equation (5.1). Included are the thresholds used for this example.

flank of a peak, the finder stores again the sample index where the threshold is crossed (i_{thr_2}). Then, it looks for the local minimum of the $\left[i_{\mathrm{thr}_1}+1,\ i_{\mathrm{thr}_2}+1\right]$ interval in the regular waveform. The index of the sample corresponding to the minimum is then saved as the preliminary location of a peak, which is used for later parameter calculations, and the finding process starts anew. If thr_2 is never crossed after the peak finder has become active, no additional information is stored. An illustration of how the difference waveform is used for peak finding is shown in figure 5.1, right. As the noise conditions in both PMT channels are found to be comparable, the same thresholds are used for all of them. The thresholds used for the summed waveform are set separately, because noise from both PMT channels is added up, which necessitates different values.

The peak finding algorithm is calibrated by running it several times over either the dataset to be analyzed or, preferably, a separate dataset taken under identical conditions, while scanning over a subset of the thr_1 and thr_2 parameter space. For each threshold value pair, the total number of peaks found in the dataset is recorded and saved into an ASCII file. The number of peaks found is then plotted against both threshold values (figure 5.2) for each channel and the summed waveform, respectively, to determine reasonable thresholds. They should be as low as possible, while being high enough to aviod identifying baseline fluctuations as peaks. According to this maxim, values for thr_1 and thr_2 are taken from points in the threshold parameter space which lie directly before the steep rise in the number of peaks found that occurs towards smaller thresholds. To confirm, that the chosen thresholds are acceptable,

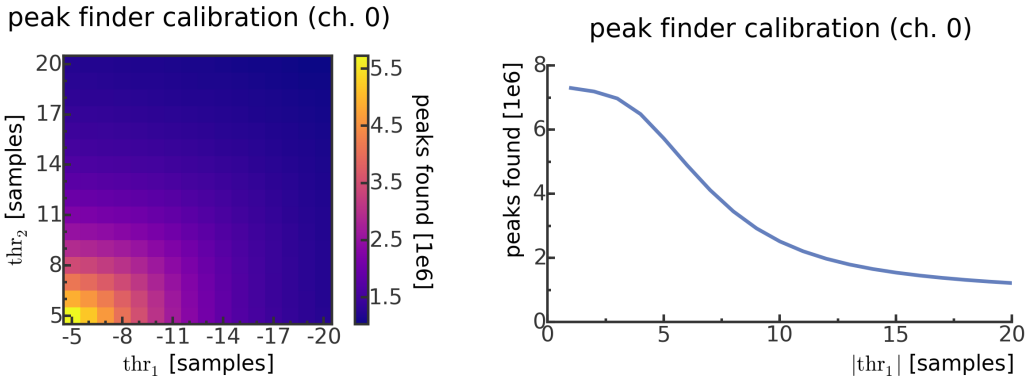

Figure 5.2.: (Left) Total number of peaks found in a dataset versus both thresholds. A steep rise in the number of peaks found towards lower threshold values is visible. (Right) Slice of the diagram to the left at $\mathrm{thr}_2 = 5$. Towards lower $|\mathrm{thr}_1|$ values, the number of peaks found first begins to rise more steeply, due to baseline fluctuations being identified as peaks. Towards even lower values, it starts to reach a plateau, as thr_2 now dominates the peak finding process.

several waveforms are looked at with walpurgisnacht's event viewer to estimate the amount of missed and wrongly identified peaks. For the datasets used in section 5.3, at least 50 events per dataset are examined, where it is found, that all peaks which caused a trigger are found by the peak finder. The amount of missed or misidentified peaks is negligible, as the vast majority of them are not visible in the waveforms of both PMT at once and belong, for reasons outlined in section 5.2.2, to a class of undesireable peaks.

After having run the peak finding algorithm once, the baseline value is estimated in the case of single channel waveforms[1]. An initial guess is made by taking the average of the first 10 waveform samples, which, due to the digitizer including a certain amount of samples occurring before the triggering signal, should in almost all cases only consist of baseline. Based on this initial guess, the extent of each peak is calculated by starting from a peak's minimum and determining the sample indices, at which the absolute difference between peak and baseline is smaller than a sample value of 4 for the first time (see figure 5.1, left). If the end of the waveform is reached without having passed the aforementioned threshold, the index of the corresponding waveform end is used. In case of reaching the minimum of another peak before passing the threshold, the index of the local maximum between the current and the other peak

[1]It is not necessary for summed waveforms, as they are constructed using baseline-corrected channel waveforms. Peak extents, as described later, are nonetheless calculated.

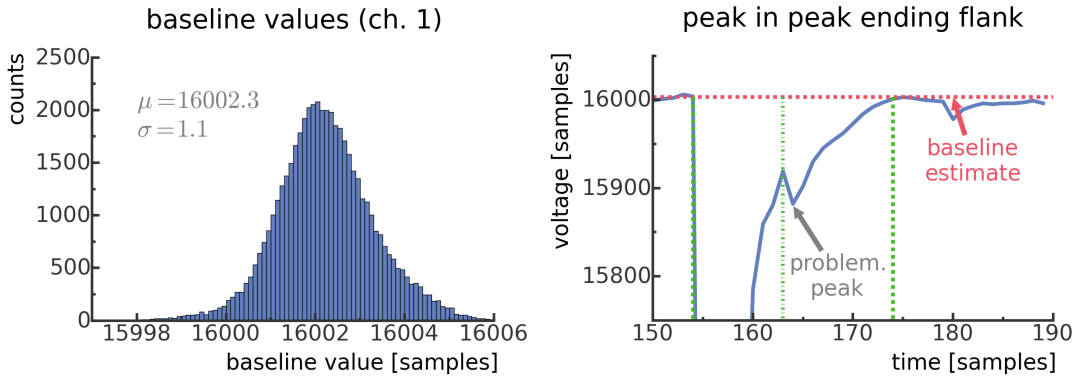

Figure 5.3.: (Left) Histogram of estimated baseline values. (Right) Example of a minor pulse within another pulse's ending flank, with vertical lines denoting peak extents. One can clearly see, that treating the minor peak as being independent would cause a chunk of the larger one to be misattributed.

is taken instead. A peak's extent is defined as the closed interval encompassed by those indices. The average of all waveform samples which do not lie within any peak's extent is then used as a new baseline estimate, and the peak extents are calculated again. This process repeats itself until either 20 iterations have passed, or the relative difference between current and previous baseline estimate is at $\mathcal{O}(10^{-12})$. At the end, the baseline-corrected channel waveforms are calculated by subtracting the respective baseline estimate from each channel waveform. The algorithm is tested by running it over a dataset containing only signal-less waveforms, obtained by triggering at random with the PMTs being turned-off (figure 5.3, right). The mean value of the resulting distribution is consistent with the baseline sample value set by the miniDAX DAQ program.

Especially in the case of larger peaks, afterpulses (see [43, section 4.3.8]) and artifacts caused by the DAQ electronics might cause an additional small peak to be located and found within a peak's ending flank (figure 5.3, right). This results in a large part of the actual peak's area to be misattributed to the smaller one. To counteract this, a peak found by the peak finder is merged with a neighboring one if all of the following criteria are met:

- The peak in question directly borders another peak, i.e. there is a match in the indices denoting the peaks' extents.
- The peak in question has a smaller absolute height ($|h|$) compared to the neighboring peak.

- The absolute difference between h and the sample value at the border between both peaks is smaller than 80 % of $|h|$. This corresponds to requiring, that both peaks are separated to a certain degree. Aforementioned percentage is determined by hand, and is found by waveform watching to merge peaks as desired.

This merging process is recursively repeated for all found peaks until no mergers take place anymore. Naturally, this possibly causes minor peaks to be wrongfully merged into a larger one. However, this is deemed as more acceptable than the case of wrongfully attributing area to a minor peak, as it is expected to be very unlikely, that signals of two real physical events overlap. This is jusitifed by observations of PMT pulse widths during LED calibration, which show, that they are typically smaller than 20 ns. Also, the lifetimes of LXe scintillation components are at the order of 30 ns [19], which limits the possible widths of scintillation signals.

In the case of afterpulse peaks, there are two classes: One class is afterpulses caused by electrons scattering off a PMT's dynode[2], which cause part of a real signal to be delayed. Thus, they have to be included in the main peak to reconstruct the full signal. The other class is afterpulses caused by ionization of residual gas inside a PMT, which should not be included, but scale with the size of the main peak preceding them [44]. Consequently, the worst case expected is a worsening of the energy resolution. Observation of PMT signals via waveform watching shows, that the vast majority of minor peaks inside the ending flank of a larger peak happens less than 100 ns after the minimum of the larger peak preceding it. As afterpulses due to gas ionization happen more than 100 ns after the peak causing them ([35, section 3.4] and [43, section 4.3.8]), it is very likely, that the vast majority of minor peaks seen in the ending flank of a peak are either caused by electron scattering afterpulses, or by electronic artifacts. Furthermore, only 1 waveform out of the more than 250 examined during peak finder validation shows an obviously incorrect merger.

The behavior of the algorithms changes slightly when ZLE (zero length encoding, see section 4.5) is used for compressing waveform data: Peak finding is done separately for each contiguous interval of valid waveform samples, equivalent to the case of separate waveforms. Baseline estimation still works as before, but only takes valid waveform samples into account.

[2] Also called "late pulses".

5.1.2. Event parameter calculation

After looking for peaks and making a baseline estimate, various peak parameters are determined. For all peaks, their area is calculated by integrating over their extents using the composite Simpson's rule for numerical integration. If the amount of samples within an extent interval is not odd, as it is required by using Simpson's rule, the trapezoidal rule is used for the interval between the last two extent samples instead. The extent is also used for calculating a peak's entropy as defined in appendix A.1, which gives a measure of whether the area of a peak is highly concentrated within only a few samples, or whether it is spread out evenly. Other important extracted parameters are a peak's height, width, and position. The peak height is defined as the peak's baseline-corrected minimum, while the peak width is defined as the length of the interval, where the peak is at 10 % of its height or "above". Lastly, the peak position is calculated by taking the weighted average of the sample index at the peak minimum and the indices of the samples bordering it, using the baseline-corrected sample values as weights.

For peaks found in the summed waveform, additional parameters are calculated. One is the integral contribution of each PMT to the peak, gained by integrating over the peak's extent separately over all channel waveforms. Another one is the coincidence level, giving the number of PMTs which have seen the peak. The coincidence level is calculated by checking, if any peaks are found in a single PMT's waveform within the extent of a summed waveform peak.

All parameter calculation algorithms are validated by generating Monte Carlo pseudo-waveforms to compare walpurgisnacht's output with that of a Python script, which utilizes SciPy [45] to recreate the parameter calculation of walpurgisnacht. The "waveforms" generated are Gaussians and triangle functions with randomized parameters, with a random constant added on top of them to represent the baseline. For peak integral and entropy calculation, dedicated SciPy functions are already available and can be directly compared to their walpurgisnacht implementations. Relative differences between processor and script outputs are $\mathcal{O}(10^{-12})$, proving that both give identical values. The calculation of peak coincidence levels is checked over the course of the waveform watching campaign for validating the peak finder (section 5.1.1).

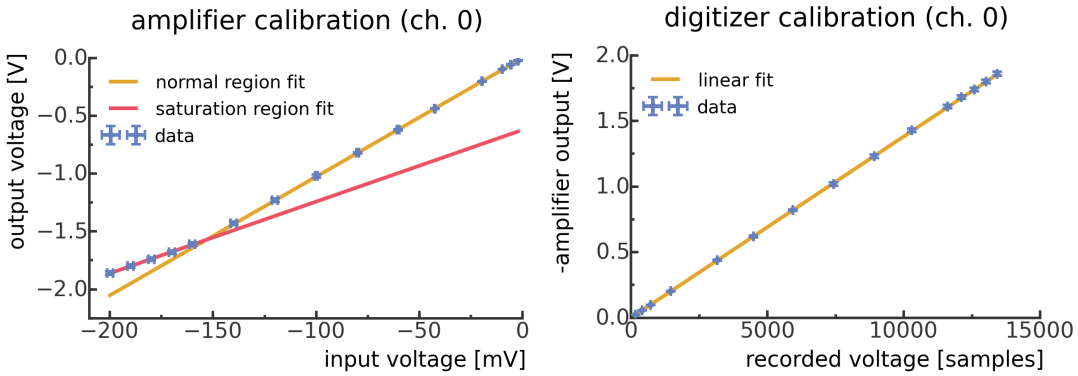

Figure 5.4.: Calibration curves of the amplifier resp. digitizer channel used for signals of the top PMT. All fits are done with linear functions.

5.2. Equipment characterization

To check their respective manufacturer specifications and to extract parameters necessary for data analysis, the amplifier, digitizer and PMTs used for DAQ are calibrated and characterized.

5.2.1. Amplifier and digitizer

Amplifier and digitizer channels are calibrated by generating rectangular pulses with varying amplitudes to be used as fake signals. Signal amplitudes before and after passing through an amplifier channel are measured with an oscilloscope, with the amplifier output also being recorded by the waveform digitizer afterwards. For each recorded rectangular pulse, the average sample value within the same part of the peak used as for the corresponding oscilloscope measurement is calculated after subtracting the baseline.

Some of the results can be seen in figure 5.4. Distortions become visible in both amplifier channels if the input voltage is smaller than $-150\,\mathrm{mV}$[3]. Also, the slope of the calibration curve is reduced by about $40\,\%$, as seen in the saturation region fit. This has to be taken into account for selecting appropriate PMT gains for the measurements in section 5.3. Other than that, both amplifier and digitizer outputs are directly proportional to their input voltages. All of the obtained proportionality constants are compatible with manufacturer specifications.

[3]For comparison, a single-photoelectron (SPE) signal has a height of about $-24\,\mathrm{mV}$ after amplification when operating the HeXe PMTs at a gain of 3×10^6.

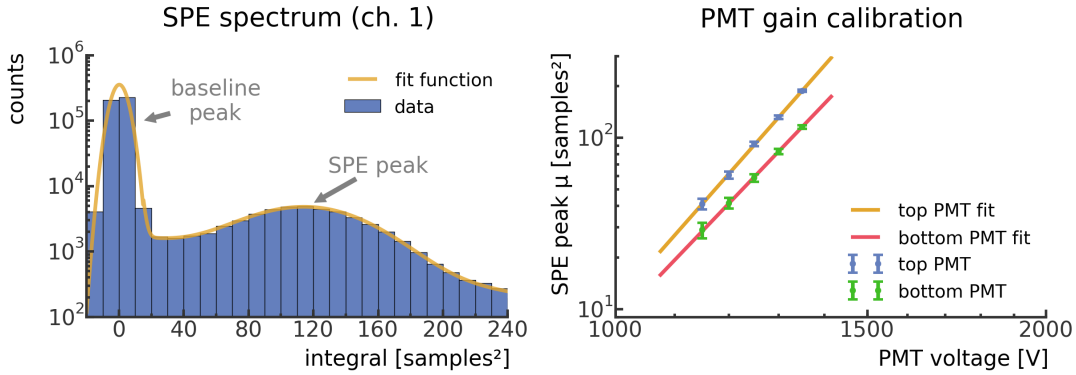

Figure 5.5.: (Left) SPE spectrum of the bottom PMT when operated at 1350 V. (Right) Double-logarithmic plot of SPE peak position versus voltage.

5.2.2. Photosensors

To obtain a PMT gain calibration curve, LED measurements at different PMT operating voltages are conducted (as described at the end of section 4.5). LED intensities are set such, that about every tenth LED pulse, a signal is seen by the PMTs. As the probability of an incident pulse to generate a certain number of photoelectrons follows a Poisson distribution, this ensures, that roughly 95 % of the observed pulses correspond to a single-photoelectron (SPE) signal.

A first data processing run allows to pinpoint the location of peaks caused by LED pulses within the recorded waveforms. For a second processing run, an interval of fixed size around this location is defined and integrated over. Finally, the average of the first and last 30 samples of a waveform is used to estimate the baseline value, which then is accordingly subtracted from the calculated integral.

The histogram of all integral values can be seen in figure 5.5, left. Two peaks can be made out. One of them is a baseline peak, which corresponds to the case of no signal being present. Due to baseline fluctuations and noise, this peak has a finite width. The other one consists of single-photoelectron (SPE) signals, with a minor amount of 2PE signals present in its right tail. A simplified and slightly modified version of the PMT response function presented in [46] is fitted onto the obtained spectra to extract the SPE peak location:

$$f(x) = N_{\mathrm{bl.}}\, e^{-\frac{1}{2}\left(\frac{x-\mu_{\mathrm{bl.}}}{\sigma_{\mathrm{bl.}}}\right)^2} + N_{\mathrm{SPE}}\, e^{-\frac{1}{2}\left(\frac{x-\mu_{\mathrm{bl.}}-\mu_{\mathrm{SPE}}}{\sigma_{\mathrm{SPE}}}\right)^2} + N_{\mathrm{2PE}}\, e^{-\frac{1}{2}\left(\frac{x-\mu_{\mathrm{bl.}}-2\mu_{\mathrm{SPE}}}{\sqrt{2}\sigma_{\mathrm{SPE}}}\right)^2} + \Theta(x-\mu_{\mathrm{exp.}})\, N_{\mathrm{exp.}}\, e^{-\alpha_{exp.}(x-\mu_{\mathrm{exp.}})} \quad (5.2)$$

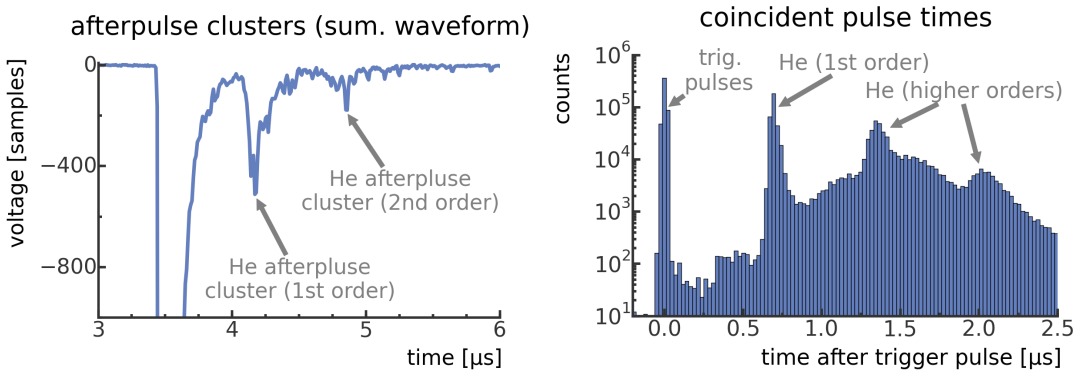

Figure 5.6.: (Left) Clusters after a major peak due to ionization of residual helium. (Right) Time spectrum of peaks seen by both PMTs. The peaks caused by residual gas afterpulses are clearly visible.

While the Gaussians in this function represent the baseline, SPE and 2PE peaks respectively, the exponential part serves as a purely phenomenological description of the valley region between baseline and SPE peak. Each fit result is, thus, being checked more carefully for possible biases or unphysical fit parameters (for ex. negative Gaussian scale factors) than usual. The extracted SPE peak locations (μ_{SPE}) are then plotted against the corresponding PMT voltages, with the result being visible in figure 5.5, right. The errors shown contain statistical errors as well as a systematic part, which is estimated by observing shifts in the peak location parameters when varying initial fit parameter values. Because the total charge inside a PMT is multiplied at each dynode stage, a power law behavior is expected [47]. Thus, the following function is fitted onto the data:

$$g(U_{\mathrm{PMT}}) = g_0 \left(\frac{U_{\mathrm{PMT}}}{U_0} \right)^p , \tag{5.3}$$

with g_0 being fixed to a target gain, such that the free parameter U_0 corresponds to the voltage needed to achieve it. As it is already implied by the aforementioned plot, the function fits perfectly to the data. When comparing the obtained values to those of previous LED calibration measurements done during the course of [35], old and new U_0 values are consistent with each other. However, the new values for p are both larger than the old ones, with the old values being, on average, 11 % smaller compared to the new ones. As the old calibration measurements have been done in a higher voltage range, this result suggests, that a pure power law might be only applicable, when looking at certain voltage ranges.

During the course of the waveform watching campaign mentioned in section 5.1.1, clusters of peaks are observed to occur at multiples of a certain, fixed time after the pulse triggering the waveform digitizer (figure 5.6). This is the typical signature of afterpulses caused by residual gas ionization in Hamamatsu R11410-10 PMTs [47], with higher order peaks existing due to afterpulses causing afterpulses themselves. It is suspected, that the PMTs are contaminated with helium, as they have been previously stored in a room, where helium has been released by accident. Furthermore, the clusters happen at multiples of about 0.7 µs. This is compatible with the expected position of helium ($\approx 0.4\,\mu s$ [47]) when taking into account, that the data of both plots in figure 5.6 has been taken at lower voltages than in [47], which causes the afterpulse peaks to be shifted towards later times. It is this kind of peaks mentioned in section 5.1.1 which has some of its sub-peaks missed by the peak finder. Due to the evidently strong contamination of both PMTs, however, a non-negligible amount of coincident, but unrelated peaks is generated. This has to be accounted for when analyzing radon data.

5.3. Measurements with radon-enriched xenon

The goal of using the HeXe system is the detection of decays from ^{222}Rn and its daughter nuclides inside LXe to gain insight in how they behave in such a medium. To achieve this, first GXe and LXe measurements are analyzed in the following section. The analysis also serves as a test of the HeXe data processor's capability of handling real data.

5.3.1. Measurement procedure

A measurement with HeXe starts by demounting the radon trap (see section 4.4) from the gas system. This is done to connect its inlet to an aqueous ^{226}Ra source, which produces ^{222}Rn. The outlet is connected to a water trap, which allows gases to flow out of the outlet, but not to flow into it. By cooling down the radon trap with liquid nitrogen and flushing helium through the ^{226}Ra source into the inlet, ^{222}Rn is carried into the radon trap and remains there due to being frozen [31]. After about 20 kBq of ^{222}Rn are within the trap, the helium is pumped out of it [31]. The trap is then again mounted onto the HeXe gas system.

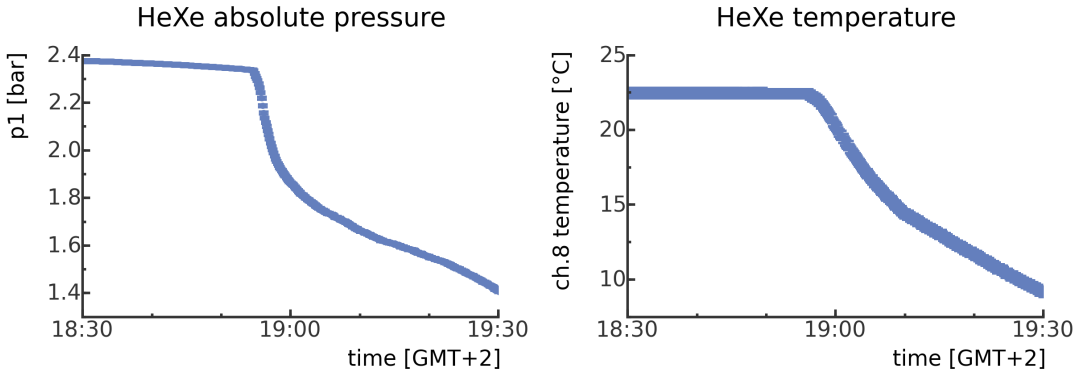

Figure 5.7.: (Left) Cryostat pressure evolution at the beginning of pre-cooling. The sudden pressure drop indicates, that liquefication has begun. (Right) Evolution of topmost PTFE Pt100 temperature (see figure 4.3). Note the temperature drop occurring shortly after liquefication has begun.

When beginning the main procedure, clean xenon is flushed through the loaded radon trap into the cryostat. Filling stops, when a pressure of 2.4 bar is reached. At this point, a GXe measurement is made at room temperature. Afterwards, the copper cold finger is cooled down to temperatures below the boiling point of xenon in a controlled way. The boiling point is at approximately −91 °C for the pressure inside the cryostat directly after filling (estimated with phase diagram from [19]). Soon after going below this temperature, a sudden pressure drop marks the beginning liquefication of xenon on the copper cold finger surface (figure 5.7, left). Because the cryostat's interior is initially at room temperature, the LXe droplets which fall into it evaporate quickly, causing it to cool down (figure 5.7, right). The cold finger temperature is then fine-tuned such, that the temperatures as seen by the Pt100 sensors inside the cryostat go down slowly enough to not damage the PMTs.

It takes about 1.5 days until the PTFE block has cooled down to temperatures close to the boiling point of xenon at the system's then current pressure. At this point, additional xenon is filled directly into the cryostat at a steady rate after letting the cold finger cool down to −107 °C, which is slightly above the freezing point of xenon [18]. The amount of time it takes for the active volume between the PMTs to be completely filled with LXe is estimated by taking the PTFE block and cryostat measures as well as the filling rate into account[4]. As a safety precaution, the recuperation bottle is immersed in liquid nitrogen to be able to immediately start recuperation. After

[4]Unfortunately, the Pt100 sensors have proven themselves to be unreliable as level meters, as LXe droplets running over them cool them down to LXe temperatures before they are actually submerged.

the desired amount of xenon is inside the cryostat, filling is stopped, and the system is left to stabilize for about an hour before an LXe measurement is taken. At the end, all of the xenon is frozen into the cooled-down recuperation bottle. A regulated, controlled flow into the bottle is maintained by letting the cold finger warm up again and switching on the cryostat's bottom plate heater.

5.3.2. Analysis and results

In this section, a pair of GXe and LXe datasets from a single HeXe measurement is analyzed in order to search for ^{222}Rn decay chain decays. The same terminology as in chapter 2 is used, i.e. signals caused by prompt scintillation light are called "S1 signals". Signal sizes are given in photons instead of PEs, as the QE values of the PMTs are accounted for. Parameters refer to peaks found in the summed waveform, unless noted otherwise.

In GXe, when operating the PMTs within the same voltage range as the one used for LED calibration, the average signal height as seen by using an oscilloscope easily exceeds the amplifier's critical voltage. Consequently, huge signal distrotions are visible. The PMTs thus have to be operated at voltages which are several hundred V lower. For checking, whether the signals of both PMTs are nonetheless properly normalized relative to each other, each S1 is plotted against its asymmetry, which is defined as in equation (3.2):

$$asym := \frac{S1_{\mathrm{top}} - S1_{\mathrm{bot.}}}{S1}.$$

$S1_{\mathrm{top}}$ and $S1_{\mathrm{bot.}}$ refer to the signal contributions by the top resp. bottom PMT in this case. Only peaks which meet the following criteria are considered:

- They have a coincidence level larger than 1, i.e. the peak finder finds a peak at the same position in both PMT channels.
- They occur within 50 ns around the average position of peaks which cause a digitizer trigger signal (see figure 5.6, right, which is created from GXe data).

Because the PMT arrangement and the active volume are symmetric and ^{222}Rn is expected to be distributed homogenously, the resulting plot should be mirror-symmetric around $asym = 0$. As it is clearly visible in figure 5.8, left, this is not the case, most likely due to the previously extracted gain fit parameters not being applicable at the low voltages the PMTs are operated at (see section 5.2.2). To correct for this, the

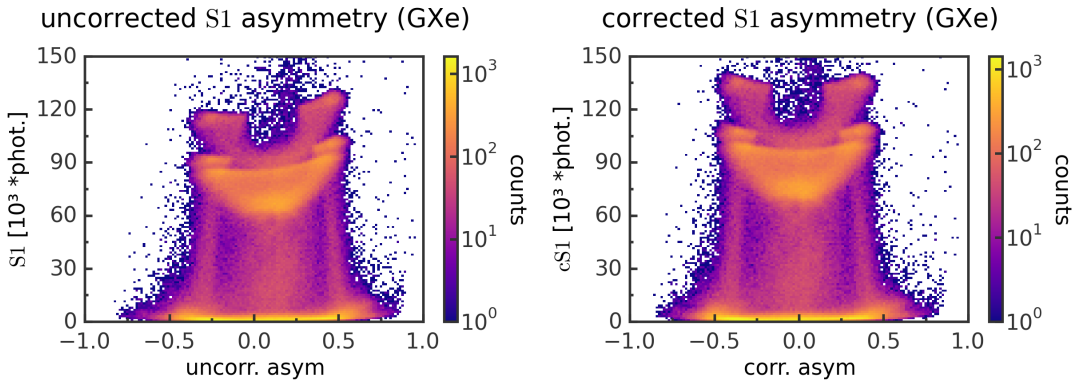

Figure 5.8.: (Left) Uncorrected S1 versus uncorrected asymmetry (GXe). (Right) S1 versus asymmetry after having applied the correction factor to the bottom PMT contribution (GXe). The structures which are visible in both plots are explained in the text.

average of $S1_{\text{top}}$ over all peaks meeting the aforementioned requirements is calculated and divided by the respective average of $S1_{\text{bot.}}$. This yields a correction factor of:

$$\frac{\mu_{S1_{\text{top}}}}{\mu_{S1_{\text{bot.}}}} = 1.27384,$$

which $S1_{\text{bot.}}$ has to be multiplied with. After applying this correction, a slight asymmetry remains (figure 5.8, right), biased towards negative values. This indicates, that the correction factor is overestimated. The most likely cause for this is, that the peak finder does not find the same amount of peaks in both channels due to gain differences. This causes the implicit S1 size cutoff resulting from the peak finder threshold to be different for both PMT channels. As a consequence, S1 sizes contain unknown systematic errors. To denote this, units of measurement which depend on PMT gain are marked with an asterisk (*) from now on.

Nonetheless, interesting structures can be seen in both asymmetry plots. At $|asym| > 0.25$ (referring to figure 5.8, right), three peaks are visible, which decrease in S1 size and get smeared out towards $asym = 0$. These peaks are suspected to belong to the α-decays of ^{222}Rn, ^{218}Po and ^{214}Po respectively. The smearing most likely results from less light being collected from decays happening in the middle of the active volume than from those happening close to a PMT. Such a position dependence on light collection is also observed in XENON100 [1]. Also, vertical lines extending downwards from the peaks are observed. They can be explained by decays, which do not deposit their entire energy into the active volume. This is mostly the case, when they

happen close to the volume's edges. Lastly, a horizontal line at S1 sizes smaller than 7.5×10^3 *phot. is seen, which could possibly belong to ^{214}Bi β-decays. Additional structures are not expected due to the large half-life of ^{210}Pb ($T_{1/2} = 22.23\,\mathrm{a}$ [23]) suppressing subsequent decays.

A subset of the S1 spectrum is selected by requiring $|asym| > 0.25$ in combination with the previous selection criteria. To prove, that the three peaks indeed belong to the aforementioned α-decays, the peaks' locations are extracted by fitting the following function, which is found to acceptably fit the data (p-value of 0.074), onto the S1 spectrum subset (figure 5.9, left):

$$f(x) := g_1(x) + g_2(x) + h_\mathrm{c}(x), \tag{5.4a}$$

with the Crystal Ball function, which is commonly used to model peak tails due to signal losses ([48, appendix E.]):

$$h_\mathrm{c}(x) := N_\mathrm{c} \begin{cases} e^{-\frac{1}{2}\left(\frac{x-\mu_\mathrm{c}}{\sigma_\mathrm{c}}\right)^2} & \text{if } \frac{x-\mu_\mathrm{c}}{\sigma_\mathrm{c}} > -\alpha_\mathrm{c} \\ A_\mathrm{c}\left(B_\mathrm{c} - \frac{x-\mu_\mathrm{c}}{\sigma_\mathrm{c}}\right)^{-n_\mathrm{c}} & \text{if } \frac{x-\mu_\mathrm{c}}{\sigma_\mathrm{c}} \leq -\alpha_\mathrm{c} \end{cases} \tag{5.4b}$$

$$A_\mathrm{c} := \left(\frac{n_\mathrm{c}}{\alpha_\mathrm{c}}\right)^{n_\mathrm{c}} e^{-\frac{1}{2}\alpha_\mathrm{c}^2} \tag{5.4c}$$

$$B_\mathrm{c} := \frac{n_\mathrm{c}}{\alpha_\mathrm{c}} - \alpha_\mathrm{c}, \tag{5.4d}$$

for modelling the rightmost peak, and:

$$g_i(x) := N_i \begin{cases} e^{-\frac{1}{2}\left(\frac{x-\mu_i}{\sigma_i}\right)^2} & \text{if } \frac{x-\mu_i}{\sigma_i} > -\alpha_i \\ e^{\frac{1}{2}\alpha^2 + \alpha\frac{x-\mu_i}{\sigma_i}} & \text{if } \frac{x-\mu_i}{\sigma_i} \leq -\alpha_i, \end{cases} \tag{5.4e}$$

which is constructed as a Gaussian-exponential hybrid based on the Crystal Ball function, to model the other two peaks. The hybrid itself and its first derivative are continuous, like it is the case with the function it is based on. For all sub-functions, the corresponding α parameters are required to be larger than 0 in order for the fit function to be well-defined. No biases, like shifts in fit function peak positions relative to peak positions in the data, are observed.

Because the rate, at which an α particle loses energy, depends on the energy it currently has, it cannot be assumed, that the amount of photons generated is directly proportional to the particle's energy. However, the stopping power for α particles in

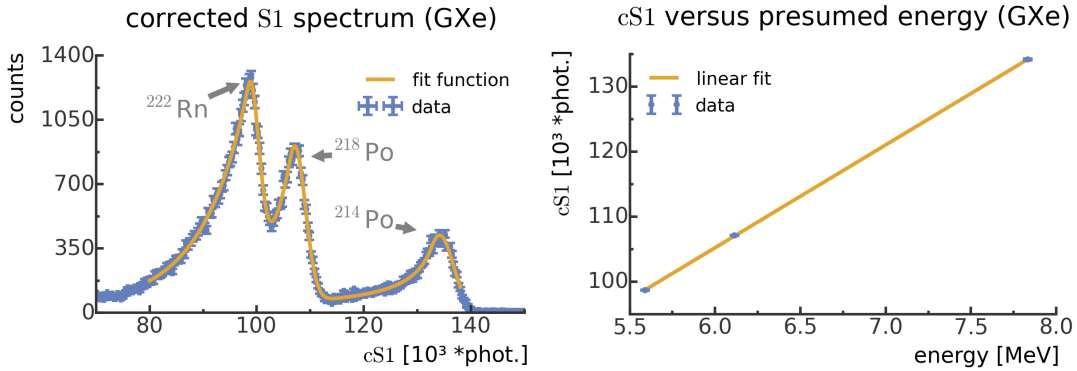

Figure 5.9.: (Left) S1 spectrum subset zoomed in on the three peaks, shown with the function for fitting the spectrum as it is described in the text (GXe). Note the peaks' tails, which are visible to their left and are most likely caused by signal losses as explained by the text. (Right) Peak positions versus presumed energies (GXe).

xenon within the expected energy range (5.59 MeV to 7.83 MeV) varies by roughly 10 % relative to the range's mean stopping power (estimated by using [49]). Thus, the photon-energy relationship within the energy interval of interest should be mostly linear. Mapping the peak with the lowest photon yield to ^{222}Rn, the one with the hightest photon yield to ^{214}Po and the remaining one to ^{218}Po, their positions in the size spectrum (the μ values from the fit) are plotted against their corresponding energies. A linear fit through the resulting three points confirms, that they lie on a single line (figure 5.9, right; p-value of 0.192), providing evidence for the peaks to be correctly matched.

More decisive evidence is obtained by looking at the presumed ^{214}Po peak. As the lifetime of ^{214}Po is by an order of magnitude smaller than the average time between waveform triggers which is observed ($\mathcal{O}(1\,\mathrm{ms})$), a corresponding correlation in time differences between recorded waveforms should be visible if the preceding decay of ^{214}Bi is recorded (BiPo coincidence). Following these observations, the distribution of time differences between an event and its predecessor is examined. The same S1 selection criteria as before are applied, including an additional condition of the S1 size to be smaller than 1.14×10^5 *phot. This should exclude most events which are triggered by an ^{214}Po-attributed S1 (see figure 5.9, left), except for parts of the distribution's tail. Another sample is selected by inverting the size criterion, meaning that events out of the presumed ^{214}Po peak are specifically selected for.

When comparing both distributions (figure 5.10), the one where the peak is removed

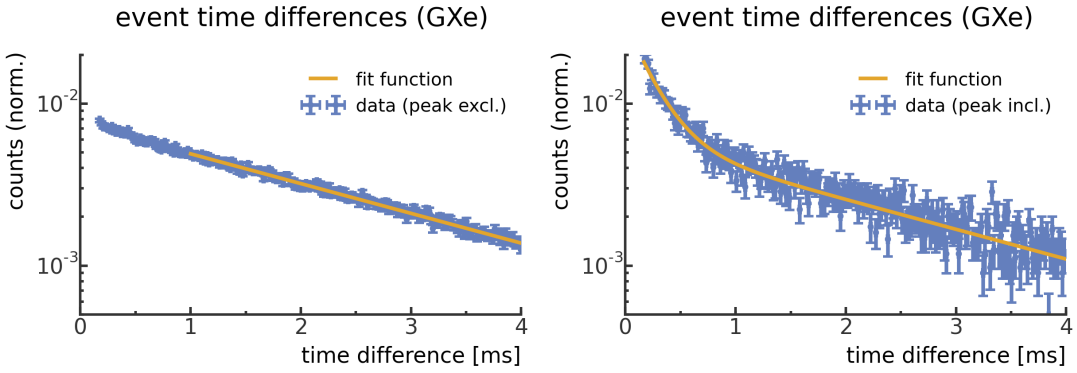

Figure 5.10.: (Left) Time differences between events following each other, excluding events from the presumed ^{214}Po peak (GXe). (Right) Same as left, but instead specifically selecting peak events (GXe).

seems to follow a pure exponential decay:

$$f(t) := N_0 e^{-\alpha_0 t}. \tag{5.5}$$

This can be explained by unrelated events occuring randomly at an average rate of α_0^{-1}, as they behave analogical to a radioactive decay. As the suspected ^{214}Po peak is not selected, unrelated events are assumed.

In the sample which specifically contains peak events, another, faster decaying exponential distribution becomes visible at small time differences, which is expected to result from the decay time distribution of ^{214}Po:

$$f(t) := N_1 e^{-\alpha_0 t} + N_2 e^{-\alpha_1 t}. \tag{5.6}$$

To check both hypotheses, two fits are made: Equation (5.5) is fitted to the sample excluding peak events (figure 5.10, left), and equation (5.6) is fitted to the sample specifically including peak events (figure 5.10, right). The value of the decay constant from the single-exponential fit (α_0) is then used to fix α_0 of the double-exponential fit. Fit ranges are chosen according to the following logic:

- The fit with equation (5.5) does not include differences smaller than 1 ms, as a residual of the second exponential distribution remains.
- Both fits should not contain empty bins.

Both times, the distributions match the data very well (p-values of 0.77 and 0.2).

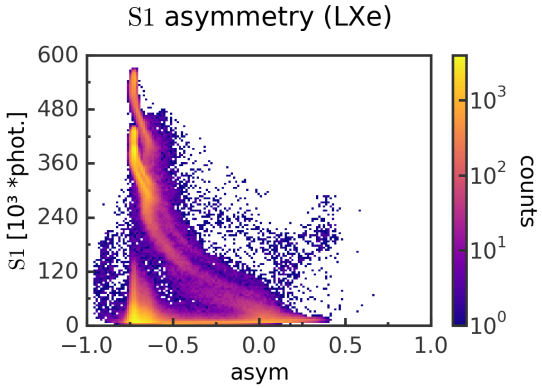

Figure 5.11.: Uncorrected S1 versus uncorrected asymmetry (LXe). Explanations for the features can be found in the text.

The single-exponential fit indeed gives a value of:

$$\alpha_0 = (423.1 \pm 1.6)\,\mathrm{Hz},$$

which is compatible with the average DAQ trigger rate that has been observed during the GXe measurement ($r = (410 \pm 15)\,\mathrm{Hz}$). This confirms, that the vast majority of events in the data sample without peak events are unrelated. This is expected for the preceding decays of ^{214}Po, because the involved half-lives are much longer (see figure 1.3) than the observed average time between events ($\mathcal{O}(1\,\mathrm{ms})$), so their decay distributions cannot be resolved. For the double-exponential fit, variations in α_1 with a magnitude of up to almost 10 % have been observed. To get a hold on this systematic uncertainty, the left integration boundary is varied up to the point, where uncorrelated events dominate, which happens at about 600 µs. Extracting α_1 and converting it to a half-life then yields:

$$T_{1/2} = (161 \pm 8_{\mathrm{stat.}} \pm 11_{\mathrm{sys.}})\,\mu\mathrm{s},$$

which is in perfect agreement with the recommended value of the ^{214}Po half-life from the Laboratorie National Henri Becquerel [23]:

$$T_{1/2}(^{214}\mathrm{Po}) = (162.3 \pm 1.2)\,\mu\mathrm{s}.$$

Combined with the results of looking at the energy-photon relationship, this gives enough evidence, that the peaks are correctly identified.

Analyzing the LXe dataset, in contrast, proves to be more challenging. Because

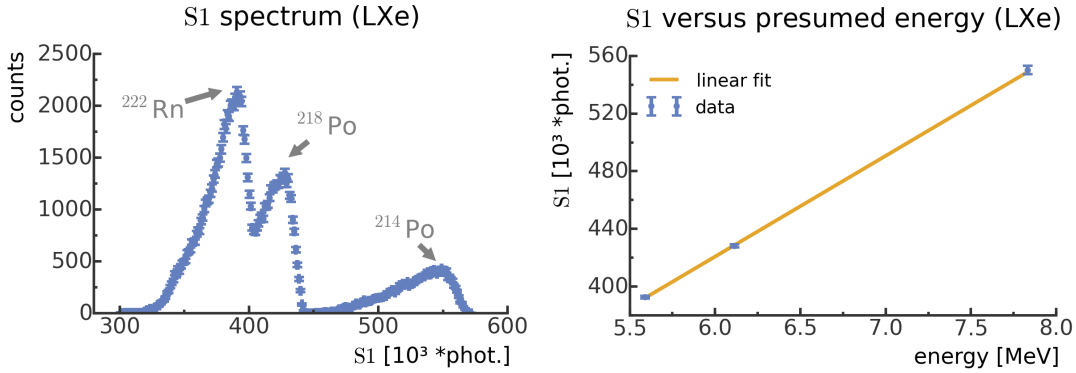

Figure 5.12.: (Left) S1 spectrum subset zoomed on the three peaks (LXe). No fit is shown, as the function used for the GXe S1 spectrum subset is unsuitable. (Right) Peak positions versus presumed energies (LXe).

average signal heights are observed to be larger than in GXe, the PMTs are operated at even lower voltages to avoid passing the critical voltage of the amplifier. Looking at $S1$ versus $asym$ (figure 5.11) reveals a distribution of events which is strongly biased towards negative asymmetries. This strongly suggests, that only the bottom PMT was submerged in LXe, while the top PMT remained in GXe. The reasoning behind this is, that the bottom PMT would see more light in this case due to light originating in LXe being reflected back at the phase boundary because of total reflection, like in XENON100 [1]. A possible explanation for only one PMT being submerged is, that the estimate for the filling time does not account for the PTFE block shrinking when cooling down.

As the assumption of both PMTs having seen the same on average cannot be made anymore, no ad hoc correction is possible for the LXe dataset. Despite that, the structures visible in the asymmetry plot are much clearer than in the GXe data. Again, three peaks are to be seen, this time at $asym < -0.71$, which get smeared out towards larger asymmetry values. The tails which extend downwards from each peak are shorter than before, which is expected due to LXe having a higher stopping power compared to GXe. In addition, a distinct population can be seen at S1 values smaller than 180×10^3 *phot., which seems likely to result from β-decays of ^{214}Bi, as it looks like a continuum.

To prove, that the peaks can again be matched to ^{222}Rn, ^{218}Po and ^{214}Po, a subset of the S1 spectrum which contains them is selected, as it is done in the GXe analysis. The subset selection criteria from the GXe analysis are modified to account for the different measurement conditions:

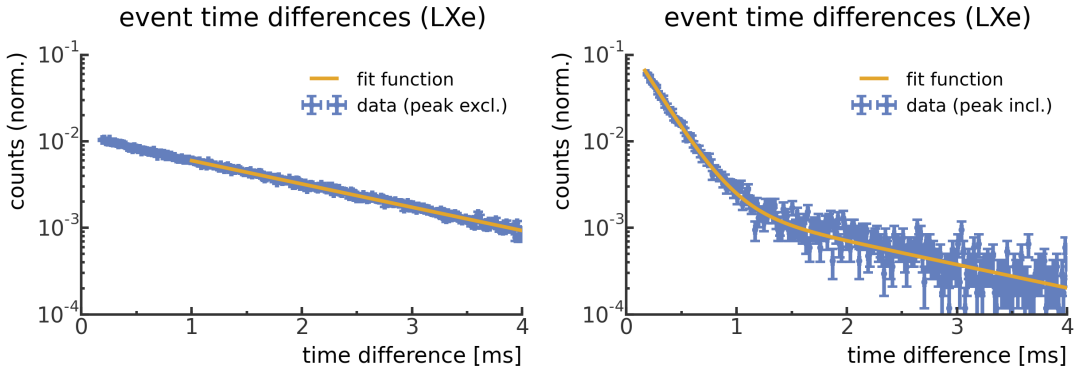

Figure 5.13.: (Left) Time differences between events following each other, excluding events from the presumed ^{214}Po peak (LXe). (Right) Same as left, but instead specifically selecting peak events (LXe).

- The S1 has a coincidence level larger than 1.
- It occurs within 60 ns around the average position of peaks causing a digitizer trigger signal.
- It has an *asym* value smaller than -0.71.

Although the ^{214}Po peak is better separated from the others compared to GXe data, likely because of the active volume's increased stopping power suppressing tails, the function used to fit the GXe S1 spectrum is unsuitable. This is even the case when replacing the Gaussian-exponential hybrid sub-functions with Crystal Ball functions. Consequently, peak positions and their errors have to be conservatively estimated by hand. The resulting fit is still acceptable (figure 5.12, right; p-value of 0.367), also when considering the fact, that due to conservative error estimates, a higher p-value is to be expected than with accurate errors.

The time difference analysis is done exactly like for the GXe dataset, except for using the updated S1 subset selection criteria and a new ^{214}Po peak boundary of 4.495×10^5 *phot. (see figure 5.12, left). The fits are still good (figure 5.13; p-values around 0.2). The extracted value for α_0:

$$\alpha_0 = (620 \pm 2)\,\mathrm{Hz},$$

is comparable with the observed DAQ trigger rate ($r = (585 \pm 15)\,\mathrm{Hz}$), and the ^{214}Po half-life extracted from α_1 is:

$$T_{1/2} = (145 \pm 2_{\mathrm{stat.}} \pm 10_{\mathrm{sys.}})\,\mu\mathrm{s},$$

which is again compatible with the value from [23], despite deviating larger from the recommended value compared to the GXe analysis.

5.4. Conclusion

First measurements with radon-enriched GXe and LXe have been performed with the HeXe system. It is found in the analysis, that distinct event populations can be made out in the S1-*asym* parameter space in GXe as well as in LXe data. Belonging to these populations are three peaks, which are shown to obey a locally linear relationship between the number of produced photons and the deposited energy when they are mapped to ^{222}Rn, ^{218}Po and ^{214}Po respectively. Furthermore, the BiPo coincidence can be observed by looking at the time difference between an event and its predecessor when selecting events within the peak attributed to ^{214}Po. The extracted ^{214}Po half-lives are:

$$T_{1/2} = (161 \pm 8_{\mathrm{stat.}} \pm 11_{\mathrm{sys.}})\,\mu\mathrm{s},$$

for the GXe dataset, and:

$$T_{1/2} = (145 \pm 2_{\mathrm{stat.}} \pm 10_{\mathrm{sys.}})\,\mu\mathrm{s},$$

for the LXe dataset. Both are compatible with the recommended value of the ^{214}Po half-life from the Laboratorie National Henri Becquerel [23]:

$$T_{1/2}(^{214}\mathrm{Po}) = (162.3 \pm 1.2)\,\mu\mathrm{s}.$$

This is enough evidence to conclude, that the HeXe system is able to detect events of the ^{222}Rn decay chain.

In addition, the analysis results also establish, that the HeXe data processor is capable of handling realistic data. This, together with the fact, that a first successful measurement has been conducted, serves as a basis for future tests.

6. Conclusion and outlook

LXe possesses properties which make it attractive for the search of hypothetical dark matter particles, like WIMPs, which are expected to only rarely interact with regular, baryonic matter. It has a relatively high density ($\rho \approx 3\,\mathrm{g/cm^3}$ [18]) combined with a high nuclear charge ($Z = 54$ [18]), meaning, that it offers many targets for particles to interact with. This is important for observing rare interactions. The same properties also cause LXe to have a high stopping power [19]. As it is a liquid, LXe also allows to construct large, homogenous detection volumina more easily [19].

Another important characteristic of xenon is, that particles interacting with it produce charge carriers and fast-response ($\mathcal{O}(20\,\mathrm{ns})$) scintillation light at the same time. Both signals are anti-correlated, which allows for an improved energy resolution as well as for interaction type discrimination [19]. The latter is especially important for dark matter direct detection experiments to reject background [1].

The above characteristics all contribute towards the success of LXe direct detection experiments like XENON100 [1] and LUX [15], which, at the time of writing, provide the best limits on WIMP masses above $6\,\mathrm{GeV/c^2}$. For future LXe experiments, like XENON1T [13], it is crucial to minimize background sources for them to be sensitive to even smaller WIMP interaction cross-sections. Of these sources, ^{222}Rn is one of the most important ones. Natural occurring ^{222}Rn within the air is able to diffuse into a detector from outside. In addition, it is also emanated by detector materials, as they contain trace amounts of ^{226}Ra and ^{238}U, which are mother nuclides of ^{222}Rn [50]. While the α-decays of the ^{222}Rn chain generate signals which can be clearly separated from nuclear recoils, which WIMPs are expected to cause, the β-decays contribute to the electronic recoil background. Even if electronic recoil events are efficiently rejected, they are able to statistically leak into the event parameter region of nuclear recoils and are thus mis-identified as a potential WIMP signal. For the XENON100 science run presented in [16], the rate of such background events in the region of interest for WIMP signals is estimated to be around 5.1×10^{-3} events/kg/day/keV. The ^{222}Rn contribution to it amounts to about 42 % [24, section 1.2.2]. This illustrates,

how important it is to reduce radon concentration levels inside a detector as much as possible. At the same time, decays of the ^{222}Rn chain have to be identified to reject them as well as to estimate the number of background events which cannot be rejected.

Previously used strategies for avoiding ^{222}Rn background might not be sufficient for future detectors to reach their targeted sensitivivies. Consequently, new techniques for the removal of ^{222}Rn are probed at the XENON100 experiment. In this particular case, a krypton distillation column, operated in reverse mode, is tested for its ability to separate radon from xenon.

To quantify the column's effectiveness, XENON100 data is used in this thesis to estimate ^{214}Po decay rates within the detector during a dedicated distillation test campaign. Because a ^{214}Po decay follows shortly after a ^{214}Bi decay ($T_{1/2}(^{214}\mathrm{Po}) = 162.3\,\mu\mathrm{s}$ [23]), they give a distinct event signature for which they can be selected for (BiPo coincidence). Based on this fact, a selection procedure for such events is devised, while accounting for acceptance losses due to the limited waveform recording time and due to the behavior of the XENON100 data processor. By using the rate estimates yielded by this method, the column is found to reduce the concentration of radon by a factor of $R = 20.3 \pm 1.9$, which is independently confirmed by another analysis which focuses on ^{222}Rn and ^{218}Po decays [31]. This result gives an incentive to further explore the usage of distillation techniques to remove radon, as future LXe experiments (for example XENON1T[13]) are likely to profit from it.

For further studies of ^{222}Rn and its daughter nuclides in LXe, a single-phase detector, called HeidelbergXenon (HeXe), has been built at the Max-Planck-Institut für Kernphysik (MPIK). It consists of two PMTs facing each other, which observe a volume of either GXe or LXe inside a small cryostat. This thesis describes the development and testing of a data processor for HeXe data analysis, the characterization of the DAQ equipment used as well as the analysis of the first available GXe and LXe data. The data processor is found to satisfactorily find peaks in recorded waveforms, with the algorithms for calculating event parameters working as desired. In the course of DAQ equipment characterization, PMTs, amplifier and digitizer behave as expected and do not show any deficiencies that would make them unsuitable for usage.

Finally, data taken with GXe and LXe is analyzed. Peaks in the pulse size spectrum are identified as belonging to the α-decays of ^{222}Rn, ^{218}Po and ^{214}Po. For both GXe and LXe data, the positions of the peaks are shown to be linearily dependent on the energies of the α-decays they belong to. In addition, the BiPo coincidence is observed,

by which values for the half-life of ^{214}Po are extracted. Both the GXe and LXe values are compatible with the value given in [23]. All in all, it is shown, that HeXe is able to detect events of the ^{222}Rn decay chain.

Furthermore, the work of this thesis establishes HeXe operation, DAQ, data processing and analysis. This allows for several future tests, like exploring the use of other radioactive sources for internal detector calibration. Other possibilities include in-situ measuring of ^{222}Rn event rates while probing radon distillation as well as adapting the system for testing new types of photosensors for usage in LXe.

A. Appendix

A.1. Peak entropy definition

Let n_0 be the index of the first sample of a peak's extent and n_f the index of the last one. With $W_{\text{nbl.}}[i]$ denoting the i-th sample of a baseline-corrected waveform, the entropy of a peak is defined as:

$$S_{\text{peak}} := -\sum_{i=n_0}^{n_f} \frac{W_{\text{nbl.}}[i]^2}{W_{\text{nbl.sum}}} \log_2\left(\frac{W_{\text{nbl.}}[i]^2}{W_{\text{nbl.sum}}}\right), \tag{A.1}$$

with

$$W_{\text{nbl.sum}} := \sum_{i=n_0}^{n_f} W_{\text{nbl.}}[i]^2. \tag{A.2}$$

It provides a measure of how much the area of a peak is spread across its extent, which can be used to discriminate between noise and actual signals.

Sources

1. Aprile, E. *et al.* The XENON100 Dark Matter Experiment. *Astropart. Phys.* **35,** 573–590 (2012).
2. Zwicky, F. Die Rotverschiebung von extragalaktischen Nebeln. German. *Helv. Phys. Acta* **6,** 110–127 (1933).
3. Rubin, V. C. & Ford, W. K. Jr. Rotation of the Andromeda Nebula from a Spectroscopic Survey of Emission Regions. *Astrophys. J.* **159,** 379–403 (1970).
4. Adam, R. *et al.* Planck 2015 results. I. Overview of products and scientific results. arXiv: `1502.01582 [astro-ph.CO]` (2015).
5. Springel, V., Frenk, C. S. & White, S. D. M. The large-scale structure of the Universe. *Nature* **440,** 1137 (2006).
6. Bertone, G. The moment of truth for WIMP Dark Matter. *Nature* **468,** 389–393 (2010).
7. Jungman, G., Kamionkowski, M. & Griest, K. Supersymmetric dark matter. *Phys. Rept.* **267,** 195–373 (1996).
8. Atwood, W. B. *et al.* The Large Area Telescope on the Fermi Gamma-ray Space Telescope Mission. *Astrophys. J.* **697,** 1071–1102 (2009).
9. Aguilar, M. *et al.* The Alpha Magnetic Spectrometer (AMS) on the International Space Station. I: Results from the test flight on the space shuttle. *Phys. Rept.* **366.** [Erratum: Phys. Rept.380,97(2003)], 331–405 (2002).
10. Aad, G. *et al.* Search for dark matter candidates and large extra dimensions in events with a jet and missing transverse momentum with the ATLAS detector. *JHEP* **1304,** 075 (2013).
11. Chatrchyan, S. *et al.* Search for dark matter and large extra dimensions in monojet events in pp collisions at $\sqrt{s} = 7$ TeV. *JHEP* **09,** 094 (2012).
12. Stolzenburg, D. Universität Wien. Private communication. 2015.

13. Aprile, E. The XENON1T Dark Matter Search Experiment. *Springer Proc. Phys.* **148,** 93–96 (2013).

14. Undagoitia, T. M. & Rauch, L. Dark matter direct-detection experiments. arXiv: 1509.08767 [physics.ins-det] (2015).

15. Akerib, D. S. *et al.* The Large Underground Xenon (LUX) Experiment. *Nucl. Instrum. Meth.* **A704,** 111–126 (2013).

16. Aprile, E. *et al.* Dark Matter Results from 225 Live Days of XENON100 Data. *Phys. Rev. Lett.* **109,** 181301 (2012).

17. Akerib, D. S. *et al.* First results from the LUX dark matter experiment at the Sanford Underground Research Facility. *Phys. Rev. Lett.* **112,** 091303 (2014).

18. Haynes, W. *CRC Handbook of Chemistry and Physics, 96th Edition* ISBN: 9781482260977 (CRC Press, 2015).

19. Aprile, E. & Doke, T. Liquid Xenon Detectors for Particle Physics and Astrophysics. *Rev. Mod. Phys.* **82,** 2053–2097 (2010).

20. Baldini, A. *et al.* Liquid Xe scintillation calorimetry and Xe optical properties. *IEEE Trans. Dielectr. Electr. Insul.* **13,** 547–555 (2006).

21. Akerib, D. S. *et al.* Radiogenic and Muon-Induced Backgrounds in the LUX Dark Matter Detector. *Astropart. Phys.* **62,** 33–46 (2015).

22. Weber, M. *Gentle Neutron Signals and Noble Background in the XENON100 Dark Matter Search Experiment* PhD thesis (Ruprecht-Karls-Universität Heidelberg, 2013). <http://hdl.handle.net/11858/00-001M-0000-0013-F898-0>.

23. Bé, M.-M. *et al.* Table of Radionuclides. <http://www.nucleide.org/DDEP_WG/DDEPdata.htm> (visited on 09/24/2015).

24. Lindemann, S. *Intrinsic ^{85}Kr and ^{222}Rn Backgrounds in the XENON Dark Matter Search* PhD thesis (Ruprecht-Karls-Universität Heidelberg, 2013). <http://hdl.handle.net/11858/00-001M-0000-0014-BD63-F>.

25. XENON100 collaboration. Measuring the radon reduction in xenon boil-off gas (working title). To be published (expected in 2015).

26. Laboratori Nazionali del Gran Sasso. <http://web.lngs.infn.it/lngs_infn/index.htm?mainRecord=http://web.lngs.infn.it/lngs_infn/contents/lngs_en/public/about/general/> (visited on 10/04/2015).

27. Hamamatsu Photonics. <http://www.hamamatsu.com> (visited on 10/02/2015).

28. Plante, G. *The XENON100 Dark Matter Experiment: Design, Construction, Calibration and 2010 Search Results with Improved Measurement of the Scintillation Response of Liquid Xenon to Low-Energy Nuclear Recoils* PhD thesis (Columbia University in the City of New York, 2012). <http://xenon.astro.columbia.edu/XENON100_Experiment/Publications/PhD_Theses.html>.
29. CAEN S.p.A. *V1724 digitizer manual* (2015). <http://www.caen.it/csite/CaenProd.jsp?parent=11&idmod=483> (visited on 08/31/2015).
30. Rosendahl, S. *et al.* A cryogenic distillation column for the XENON1T experiment. *J. Phys. Conf. Ser.* **564,** 012006 (2014).
31. Brünner, S. Max-Planck-Institut für Kernphysik. Private communication. 2015.
32. XENON collaboration. Private communication. 2015.
33. Arduino LLC & Arduino S.r.l. <http://www.arduino.cc> and <http://www.arduino.org>.
34. Aprile, E. *et al.* Lowering the radioactivity of the photomultiplier tubes for the XENON1T dark matter experiment. arXiv: 1503.07698 [astro-ph.IM] (2015).
35. Cichon, D. *Examining Hamamatsu R11410-21 photomultipliers for XENON1T at room and liquid Xenon temperatures* Bachelor's Thesis (Ruprecht-Karls-Universität Heidelberg, 2013). <http://hdl.handle.net/11858/00-001M-0000-0014-4825-A>.
36. iseg Spezialelektronik GmbH. <http://iseg-hv.com>.
37. Phillips Scientific. <http://www.phillipsscientific.com>.
38. Technoland Corporation. <http://www.tcnland.co.jp/index_e.html>.
39. National Instruments Corporation. <http://www.ni.com>.
40. Raspberry Pi Foundation. <http://www.raspberrypi.org>.
41. PostgreSQL. <http://www.postgresql.org>.
42. CERN. *ROOT* <http://root.cern.ch>.
43. Hamamatsu Photonics. *Photomultiplier Tubes - Basics and Applications* 3a. <http://www.hamamatsu.com/resources/pdf/etd/PMT_handbook_v3aE.pdf> (visited on 09/14/2015) (Aug. 2007).
44. Baudis, L. *et al.* Performance of the Hamamatsu R11410 Photomultiplier Tube in cryogenic Xenon Environments. *JINST* **8,** P04026 (2013).
45. Jones, E., Oliphant, T., Peterson, P., *et al. SciPy: Open source scientific tools for Python* 2001-present. <http://www.scipy.org/> (visited on 09/21/2015).

46. Bellamy, E. H. *et al.* Absolute calibration and monitoring of a spectrometric channel using a photomultiplier. *Nucl. Instrum. Meth.* **A339,** 468–476 (1994).

47. Lung, K. *et al.* Characterization of the Hamamatsu R11410-10 3-Inch Photomultiplier Tube for Liquid Xenon Dark Matter Direct Detection Experiments. *Nucl. Instrum. Meth.* **A696,** 32–39 (2012).

48. Skwarnicki, T. *A study of the radiative CASCADE transitions between the Upsilon-Prime and Upsilon resonances* PhD thesis (Cracow, INP, 1986). <`http://lss.fnal.gov/cgi-bin/find_paper.pl?other/thesis/skwarnicki.pdf`>.

49. Berger, M., Coursey, J., Zucker, M. & Chang, J. ESTAR, PSTAR and ASTAR: Computer Programs for Calculating Stopping-Power and Range Tables for Electrons, Protons and Helium Ions (version 1.2.3). <`http://physics.nist.gov/Star`> (visited on 09/24/2015).

50. Aprile, E. *et al.* Study of the electromagnetic background in the XENON100 experiment. *Phys. Rev.* **D83.** [Erratum: Phys. Rev.D85,029904(2012)], 082001 (2011).

Erklärung:

Ich versichere, dass ich diese Arbeit selbstständig verfasst und keine anderen als die angegebenen Quellen und Hilfsmittel benutzt habe.

Heidelberg, den 06.10.2015 .....